



Norwegian University of
Science and Technology

Automation of CFD Analysis in Waterways

**Andreas Sætre
Hammerlund**

Master of Science in Mechanical Engineering

Submission date: June 2016

Supervisor: Pål Tore Selbo Storli, EPT

Norwegian University of Science and Technology
Department of Energy and Process Engineering

EPT-M-2016-49

MASTER THESIS

for

Student

Andreas Sætre Hammerlund

Spring 2016

Automation of CFD Analysis in Waterways

*Automatisering av CFD analyse i vannveier***Background and objective**

The need for accurate simulation results are increasing as the general performance expectancy in the society increase. In the hydropower industry, simple one-dimensional analysis on fluid dynamics are becoming too simple obtain the level of detail necessary to move the development further. However, more accurate tools that provide the desired level of detail, Computational Fluid Dynamics (CFD), require a lot of user knowledge related to the tool itself. This knowledge takes a lot of time to gain, and when such results are only desired from time to time, the threshold for obtaining the necessary knowledge is high. To complicate matters even further, the tools are expensive and require a lot of computing power, representing resources that are hard get internally in the power companies.

Statkraft together with EDR Medeso have initiated an R&D project, which will develop an online service available on demand where it is possible to set up geometry for simulations using a Graphical User Interface (GUI). This service will require no knowledge on how to perform a CFD analysis. In order for this to be possible, the CFD analysis performed based on the GUI inputs need to be robust, fast and accurate according to user specifications.

The objective of the master work will be to create CFD tool elements that can be used for such a service. The CFD tools must be verified against empirical knowledge, and if possible experimental results.

The following tasks are to be considered:

1. Literature study on CFD numerical calculations and investigating the potential of reducing computational effort without loss of accuracy (?)
2. Together with supervisors, agree on certain simulation cases that will be the objective for further and more detailed investigations:
 - a. Establish a robust mesh generation procedure including mesh independence testing
 - b. Establish robust solutions for generating reliable boundary conditions for the objective cases, including investigation of simulations using actual roughness vs. simulations using a smooth pipe and a friction factor implying roughness
 - c. Establish a robust solution for including free water surfaces in simulations
 - d. Post processing of results to indicate where particles will travel in the system
3. Verify the solution against empirical relations or available measurements

-- " --

Within 14 days of receiving the written text on the master thesis, the candidate shall submit a research plan for his project to the department.

When the thesis is evaluated, emphasis is put on processing of the results, and that they are presented in tabular and/or graphic form in a clear manner, and that they are analysed carefully.

The thesis should be formulated as a research report with summary both in English and Norwegian, conclusion, literature references, table of contents etc. During the preparation of the text, the candidate should make an effort to produce a well-structured and easily readable report. In order to ease the evaluation of the thesis, it is important that the cross-references are correct. In the making of the report, strong emphasis should be placed on both a thorough discussion of the results and an orderly presentation.

The candidate is requested to initiate and keep close contact with his/her academic supervisor(s) throughout the working period. The candidate must follow the rules and regulations of NTNU as well as passive directions given by the Department of Energy and Process Engineering.

Risk assessment of the candidate's work shall be carried out according to the department's procedures. The risk assessment must be documented and included as part of the final report. Events related to the candidate's work adversely affecting the health, safety or security, must be documented and included as part of the final report. If the documentation on risk assessment represents a large number of pages, the full version is to be submitted electronically to the supervisor and an excerpt is included in the report.

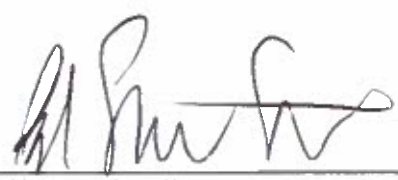
Pursuant to "Regulations concerning the supplementary provisions to the technology study program/Master of Science" at NTNU §20, the Department reserves the permission to utilize all the results and data for teaching and research purposes as well as in future publications.

The final report is to be submitted digitally in DAIM. An executive summary of the thesis including title, student's name, supervisor's name, year, department name, and NTNU's logo and name, shall be submitted to the department as a separate pdf file. Based on an agreement with the supervisor, the final report and other material and documents may be given to the supervisor in digital format.

- Work to be done in lab (Water power lab, Fluids engineering lab, Thermal engineering lab)
 Field work

Department of Energy and Process Engineering, 15. January 2016


Olav Bolland
Department Head


Pål-Tore Storli
Academic Supervisor

Research Advisor:
Martin Aasved Holst

Preface

This Master's thesis was written at the Waterpower Laboratory at Norwegian University of Science and Technology during the spring of 2016. The work was performed in collaboration with the technology company EDR Medeso. The objective of the Master's work was to develop and perform thoroughly testing of numerical methods for an automated CFD application. The work has been challenging, but most of all educative and inspiring.

I would like to thank EDR Medeso for the opportunity to join such an interesting project and I hope that my work has contributed to the development of the automated CFD application. My supervisor at EDR Medeso, Martin Aasved Holst, deserves my gratitude for his valuable support throughout the semester. I would also like to thank my supervisor at NTNU, Pål-Tore Storli, for his support regarding the writing of the report.

At last, but not least, I am grateful for being a part of the student environment at the Waterpower laboratory. It has been a great way to finish my studies at NTNU.

Andreas S. Hammerlund

Andreas Sætre Hammerlund

Trondheim, June 13, 2016

Abstract

The objective of this Master's work have been to develop robust numerical methods for an online, automated application for Computational Fluid Dynamics (CFD) analyses of details in the hydropower waterways. This has involved thoroughly testing of several approaches regarding mesh generation, implementation of rough surfaces and sediment transport, as well as alternatives to inlet boundary conditions. The analyses have shown that it should be possible to obtain representative results in order to get a conceptual understanding of the flow in the different component of hydropower waterways.

The mesh resolution studies' aim was to find a "rule of thumb" regarding an acceptable mesh resolution. Several geometries was analysed, and a starting point with regards to mesh resolution was given by the ratio "hydraulic diameter / body size of mesh element". However, as the geometries studied with the automatic CFD application may vary in complexity, it is recommended to implement a mesh dependence test in the automated CFD application. A validation of the method regarding mesh resolution was performed of the sand trap in Tonstad Hydropower station. The velocity profiles at three locations in the sand trap compared well with the results of field measurements.

In the roughness studies it was confirmed that the built in rough wall models in ANSYS CFX was not applicable for the large scale roughness in blasted hydropower waterways. Simulations of geometries with physical roughness elements provides acceptable results for pressure loss compared to hand calculations based on empirical formulas. However, due to mesh requirements, the computational cost is not within the limits of an automated CFD application. A cost efficient method regarding mesh deformation in order to create a rough surfaced domain, showed promising results. However, this method will need some modifications in order to be robust and applicable in automated applications.

Implementation of sediment transport by Eulerian-Lagrangian particle tracking seem to give acceptable results when modelling particles suspended in the flow, but the model fails to capture the resuspension of particles that has been in contact with the bottom. However, in combination with the velocity and shear stress data from the regular automated CFD analyses, it is possible to obtain a good understanding of the particle transport capability of the flow.

Sammendrag

Formålet med denne masteroppgaven har vært å utvikle robuste numeriske metoder som skal brukes i en nettbasert automatisert applikasjon for numeriske strømningsanalyser (CFD) av detaljer i vannveiene i et vannkraftverk. Dette har involvert grundig testing av forskjellige framgangsmåter når det gjelder generering av mesh, implementasjon av ruhet på vegger, sedimenttransport og muligheten til å bruke trykk som grensebetingelse for innløpet. Analysene har vist at en automatisert CFD applikasjon kan oppnå representative resultater for å gi en konseptuell forståelse for strømmingen i forskjellige vannveiskomponenter.

Målsettingen med mesh-studiene var å finne en tommelfingerregel for en akseptabel meshoppløsning. Flere geometrier ble analysert og det ble foreslått et utgangspunkt for meshoppløsning gitt ved forholdet mellom hydraulisk diameter og cellestørrelse. Siden utvalget av geometrier som kan genereres i den automatiserte CFD applikasjonen kan ha variert grad av kompleksitet, er det anbefalt å implementere en form for mesh-uavhengighetstest i applikasjonen. For å validere metoden ble det utført analyser av et sandfang i Tonstad kraftverk og sammenlignet med måledata. Hastighetsmålinger fra tre lokasjoner i sandfanget viste seg å stemme godt overens med måledataene.

I ruhetsstudiet ble det bekreftet at de innebygde modellene for ruhet i ANSYS CFX ikke er gyldige for størrelsen på ruhetselementene i råsprengte vannveistunneler. Simuleringer utført på tunneler med fysiske ruhetselementer gir gode resultater for trykktap sammenlignet med empiriske formler. Riktignok er kravene til finhet på meshet i slike analyser for omfattende til at metoden kan benyttes i den automatiserte applikasjonen. En annen og mindre ressurskrevende metode går på skape et domene med ruhetselementer ved hjelp av deformasjon av meshet. Analysene ga lovende resultater, men krever noen modifikasjoner og videreutvikling for gi ønsket grad av robusthet for å være aktuell for den automatiserte applikasjonen.

Implementasjon av sedimenttransport ved bruk av *Eulerian-Lagrangian particle tracking* så ut til å gi akseptable resultater for suspendert sedimenttransport, men modellen mislykkes på å gjenskape et realistisk bilde av partikkeltransporten langs bunnen. Det er imidlertid mulig å tilegne seg en forståelse for strømmens partikkeltransportevne ved å analysere hastighets og skjærspenningsresultatene gitt i den vanlige CFD-analysen.

Table of Contents

List of Figures	ix
List of Tables.....	xi
Nomenclature	xiii
1 Introduction	1
1.1 Background.....	1
1.2 Objective.....	2
1.3 Outline	2
2 Previous Work.....	5
3 Theory	9
3.1 A Hydropower Plant.....	9
3.2 Internal Flow.....	12
3.3 Sediment Transport.....	14
3.4 Roughness Estimation	17
4 CFD Theory and ANSYS CFX.....	19
4.1 Meshing	20
4.2 Turbulence	22
4.3 Pressure Representation in ANSYS CFX.....	23
4.4 Wall Functions.....	24
4.5 Rough Wall Modelling in CFD	25
4.6 Particle Tracking in ANSYS CFX.....	27
4.7 Errors and Uncertainties in CFD	28
5 Automated CFD Application	31
5.1 Initial Validation of the CFX Solver	32
6 Mesh Resolution Study	35
6.1 Test Geometry 1 – Tunnel to Pipe.....	35
6.2 Test Geometry 2 - Nore Upper Sand Trap	42
6.3 Test Geometry 3 - Nore Lower Sand Trap	46
6.4 Conclusion of the Mesh Resolution Study	50
7 CFD Analyses of Rough Surfaces.....	51
7.1 MATLAB Generated Rough Geometry	52
7.2 Mesh Deformation to Simulate Roughness	59
7.3 Conclusion of the Roughness Studies	62

8	Sediment Transport	63
8.1	Test Geometry 3 – Sediment Transport Study	63
8.2	Test Geometry 2 – Sediment Transport Study	66
8.3	Conclusion to the Sediment Transport Study	69
9	Pressure Inlet	71
9.1	Geometry, Meshing and Setup	71
9.2	Results and Discussion	73
10	Validation Case	75
10.1	Geometry, Meshing and Setup	75
10.2	Results and Discussion	77
11	Conclusion and Further work	81
	Bibliography.....	83
Appendix A	MATLAB Roughness Code	85
Appendix B	Head Loss Coefficients.....	87
Appendix C	Statkraft Drawings	89
Appendix D	Total Pressure Cone Shape	91

List of Figures

- Figure 1.1 Graphical description of the structure of this report. 3
- Figure 3.1 Principal sketch of a hydropower plant. 9
- Figure 3.2 Low head hydropower plant 10
- Figure 3.3 Typical cross sectional shape of a blasted hydropower tunnel 10
- Figure 3.4 Principal sketch of a sand trap 11
- Figure 3.5 Shield's diagram for movement of bottom particles 16
- Figure 3.6 Hjulström’s diagram 16
- Figure 3.7 Tunnel roughness estimation by the IBA method 18
- Figure 4.1 Cell centered and vertex centered numerics 19
- Figure 4.2 Mesh element shapes in ANSYS CFX 21
- Figure 4.3 Overview of the ANSYS CFX mesh quality measures 21
- Figure 4.4 Turbulence time averaging 22
- Figure 4.5 Turbulence velocity profile..... 24
- Figure 4.6 Different approaches to the rough wall modelling in CFD applications 26
- Figure 4.7 Downward shift of the Logarithmic Velocity Profile in ANSYS CFX 26
- Figure 5.1 Geometry of the simple pipe-to-pipe connection..... 32
- Figure 5.2 Study of a pipe-to-pipe connection with a sudden contraction..... 33
- Figure 6.1 Test Geometry 1 – Tunnel to pipe geometry. 36
- Figure 6.2 Mesh dependence test of Test Geometry 1. 38
- Figure 6.3 Monitor plot of the inlet pressure fluctuations..... 39
- Figure 6.4 Results of the y^+ sensitivity studies 40
- Figure 6.5 Mesh dependence test of Test Geometry 1 41
- Figure 6.6 Test Geometry 2 – A sand trap in Tonstad Hydropower station. 42
- Figure 6.7 Capture of the mesh around the corner of the sand trap of Test Geometry 2. 43
- Figure 6.8 Normalised pressure drop in Nore upper sand trap. 44
- Figure 6.9 Velocity contour plot of the flow in Test Geometry 2..... 45
- Figure 6.10 Test Geometry 3 - Nore lower sand trap..... 47
- Figure 6.11 Velocity contour plot of the flow in Test Geometry 3..... 49
- Figure 6.12 Pressure loss from inlet to the three different outlets at Nore lower sand trap..... 49
- Figure 7.1 Blasted tunnel geometry replica created in MATLAB 53
- Figure 7.2 Cross sectional view of the mesh in the MATLAB generated geometry. 54

Figure 7.3 Zoomed in on the mesh around a roughness element	55
Figure 7.4 Cross section velocity contour plot of the MATLAB geometry.....	57
Figure 7.5 Longitudinal contour plot of turbulence kinetic energy	58
Figure 7.6 Cross section turbulent kinetic energy contour plot	58
Figure 7.7 Domain representation of the simulation with mesh deformation.....	60
Figure 7.8 Capture of the mesh around the roughness elements.....	60
Figure 7.9 Velocity contour of the SST steady state simulations	61
Figure 8.1 Particle trajectories of the particles released on Test Geometry 3.....	65
Figure 8.2 Contour plot of the shear stress on the bottom of Test Geometry 2.	67
Figure 8.3 Particle trajectories of particle with different diameters in Test Geometry 2.....	68
Figure 9.1 Illustration of the geometries used in the total pressure inlet study.....	72
Figure 9.2 Comparison of cone and box inlet.	73
Figure 9.3 Contour plot of turbulence intensity development	74
Figure 9.4 Zoomed in on the geometry of interest. Turbulent kinetic energy.	74
Figure 10.1 Geometry of one of the sand traps at Tonstad hydropower station.	76
Figure 10.2 Comparison of ADCP 1 velocity measurements and CFD results.	78
Figure 10.3 Comparison of ADCP 2 velocity measurements and CFD results.	78
Figure 10.4 Comparison of ADCP 3 velocity measurements and CFD results.	78
Figure 10.5 Velocity monitor points at the centre of the cross sections	79
Figure 11.1 Loss coefficient for the sudden contraction of a pipe.	87
Figure 11.2 Loss coefficients for a rounded inlet.....	87
Figure 11.3 Head loss coefficient for a pipe reducer.	87
Figure 11.4 Head loss coefficient for a gradual expansion of a pipe.	87
Figure 11.5 Descriptive sketch of total pressure inlet geometry.....	91

List of Tables

Table 4.1 ANSYS CFX Mesh quality measures 21

Table 4.2 Types of errors and uncertainties in CFD analyses [24]. 29

Table 6.1 Mesh details of Test Geometry 1 37

Table 6.2 Mesh details of Test Geometry 2. 43

Table 6.3 Mesh details of Test Geometry 3 47

Table 6.4 Ratio of hydraulic diameter of cross section versus required body size 50

Table 7.1 Mesh details of the MATLAB generated rough geometry analyses. 54

Table 7.2 Results of the analyses on the rough tunnel geometry created in MATLAB. 57

Table 7.3 Pressure drop in analysis of rough surfaces by mesh deformation. 61

Table 8.1 Particle statistics of the analyses of Test Geometry 3. 65

Table 8.2 Particle statistics of the analyses on Test Geometry 2. 67

Table 10.1 Mesh details of the sand trap analysis of Tonstad Hydropower plant. 76

Nomenclature

Symbols		Acronyms	
A_c	Cross section area	ADCP	Acoustic Doppler Current Profiler
C_s	Shields number	CFD	Computational Fluid Dynamics
D_c	Critical diameter for particle movement	DES	Detached Eddy Simulations
D_h	Hydraulic diameter	LES	Large Eddy Simulations
D_p	Particle diameter	NTNU	Norwegian University of Science and Technology
f	Darcy friction factor	RANS	Reynold-Averaged Navier-Stokes
g	Acceleration of gravity	SAS	Scale Adaptive Simulations
h_l	Head loss	SST	Shear Stress Transport
h_f	Head loss due to friction	TG1,2,3	Test Geometries 1, 2 and 3
h_s	Head loss due to minor losses	VC	Validation Case
k	Head loss coefficient		
k_s	Roughness height		
L	Length		
M	Manning number		
P	Pressure		
P_w	Wetted Perimeter		
r	Radius		
R_h	Hydraulic radius		
Re	Reynolds number		
rms	Root mean square		
u	Water velocity		
u_*	Shear velocity of water		
u_t	Friction velocity of water		
V	Water velocity		
y^+	Non dimensional wall normal distance		
z	Height level, elevation		
			Greek symbols
		α	Expansion and contraction angle
		ϵ	Turbulent dissipation
		λ	Wavelength
		μ	Dynamic viscosity
		ν	Kinematic viscosity
		ρ	Density of water
		ρ_s	Density of sand
		τ	Shear stress
		τ_c	Critical shear stress
		ω	Turbulent frequency

1 Introduction

With increasing population and industrialisation, the world's demand for energy is growing every day. On the UN climate conference in Paris in the autumn of 2015, politicians from all corners of the world agreed on the two-degree target of global warming [22]. In order for this to be realisable, “dirty” sources of energy, such as coal and hydrocarbons, has to be replaced by renewable solutions. Hydropower is a clean source of renewable energy. In 2013, approximately 15 percent of the total electricity production worldwide comes from hydropower [25]. The fact that the areas with the biggest unutilised potentials of hydropower, such as South America, Asia and Africa, also has the biggest increase in energy demand, makes hydropower very good candidate as source of energy [14]. In Norway, hydropower constitutes for 99 percent of the total power production and is an important part of the Norwegian industry. This spring, the Norwegian government released a White Paper on energy policy towards 2030 [10]. It was emphasised that hydropower as source of energy will be even more important in the future.

1.1 Background

The development and maintenance of hydropower plants is a thorough process involving analyses based on both theoretical and empirical knowledge. As geometries become complex, pressure loss and sediment transport get difficult to calculate. Therefore, big and costly decisions regarding geometry are often based on “a good guess”. The application of Computational Fluid Dynamics (CFD) has become a popular and valuable tool to perform such analyses. However, CFD analyses require extensive knowledge of both software and fluid mechanics. As external consultancy support may be required, application of CFD is often considered too expensive for simple waterway analyses.

EDR Medeso, in collaboration with Statkraft, is working on an automated application where the user through an online service can perform CFD analyses on details in the hydropower waterways. An intuitive interface will help the user to design a system of predefined waterway components in order to represent the desired system. By specifying type of geometry and physical measures, the range of different systems that can be analysed is wide. The user will not be required to inherit extensive computational resources or prior knowledge of CFD, in order to perform the analyses. The process of geometry generation, meshing, setup and

execution of the analysis is performed automatically at a remote computer. When the analyses are finished, a report with predefined structure will be sent to the user by email. The report will include figures and tabulated data regarding velocity, pressure and particle transport in the analysed domain.

1.2 Objective

Hopefully, the easiness and cost efficiency of the analyses will make the usage of CFD tools more applicable to Statkraft and other companies. However, in order for such an automated CFD application to be reliable, thorough testing is required. This master's work will look into the testing and verification of the building of the geometry, mesh generation and setup of the CFD model.

1.3 Outline

A figurative representation of the outline of this thesis is given in Figure 1.1. Following this introduction chapter, previous work on analyses of waterways will be presented. Chapter 3 contains a presentation of relevant theory related to hydropower systems and how different waterways properties can be analysed using CFD software. Chapter 4 will include general information of CFD theory and details of the chosen CFD software, ANSYS CFX. The chapters 5-10 constitutes the main part of this master's thesis. Information about the automated solver will be given in Chapter 5, together with an initial validation of the CFX solver. As the geometries that can be built in the automated CFD application can be of a wide range of complexity, the meshing process is a critical stage of the process to obtain reliable results. Therefore, Chapter 6 will address the issues regarding the development of a robust mesh generation. Chapter 7 will include the implementation of rough walls and Chapter 8 regards the analysis of sediment transport in the waterways. Different types of input parameters might be desirable in the automated CFD application. Therefore, the investigation of including pressure as input parameter is presented in Chapter 9. In Chapter 10, a part of the waterways of Tonstad hydropower station is analysed according to the findings in the previous chapters as a validation of the automated CFD approach. A conclusion will be given at the very end of the thesis.

Task 1 of the master assignment text is primarily covered in the chapters 2 and 4, while the chapters 5-10 covers Task 2 and 3. However, Task 2 c), regarding the implementation of free water surfaces in the CFD application, is not answered in agreement with the supervisors. The

subject is highly relevant, but as the development of the automated CFD application is at an early stage, such complex phenomena are not prioritised at the moment.

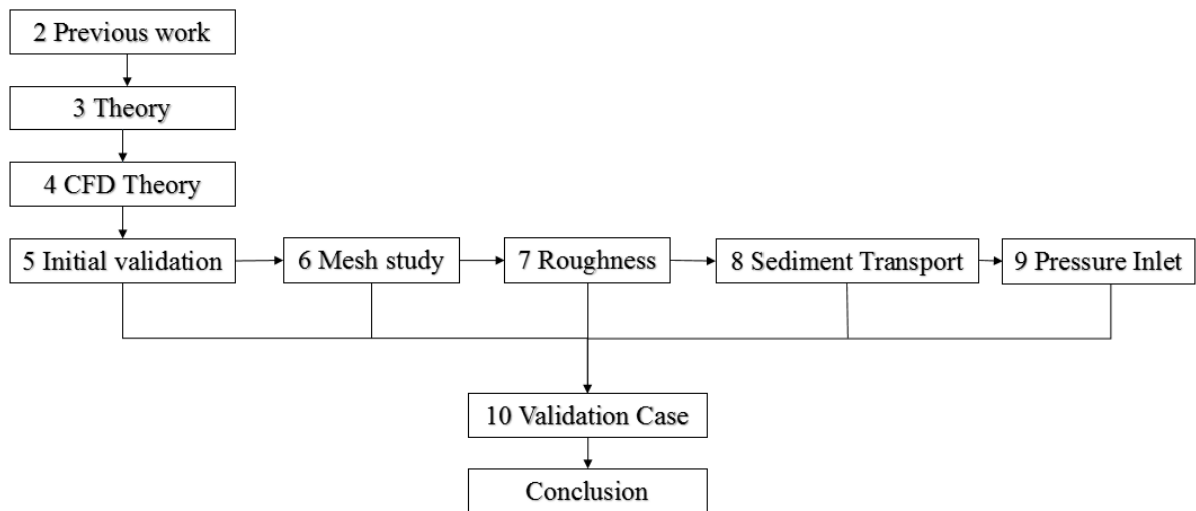


Figure 1.1 Graphical description of the structure of this report.

2 Previous Work

The design of waterways in hydropower systems are based on estimate formulas and empirical knowledge. Formulas for friction loss provide good estimates regarding head loss and dynamic analyses can be performed for instance using the software application LVTrans. LVTrans is a LabView program package developed for hydropower waterway analyses. The program performs one-dimensional transient analyses based on user input. The user designs a system by selecting components from a predefined library. Parameters, such as length, cross-sectional area, friction, mass flow and elevation, are specified before the simulation begins. This type of setup has inspired the interface in the planned automated CFD application. Even though the automated CFD analyses will regard details of the waterways only, a further extension to the work could be to link the local 3D CFD analyses to the global 1D analyses of LVTrans and similar.

CFD Analyses of Waterways

Empirical formulas for friction loss provide a good estimate regarding pressure losses and LVTrans provides information about the oscillations of a running system. However, the analysis is only one dimensional and development of CFD analyses have made it possible to perform more detailed 3D analyses on selected parts of the waterways. 3D CFD analyses of a whole waterways system demand an excessive amount of computational resources. Hence, CFD will not, in nearest future, replace the one-dimensional analyses of a whole waterways system. However, CFD makes it possible to analyse local effects, such as intakes, spillways, sand traps and other complex geometry sections of the waterways.

At NTNU there have been performed CFD analyses of waterways. Oddmund Brevik performed both steady state and transient simulations of a sand trap at Tonstad hydropower station [5]. He analysed both stationary flow and a filling situation to determine if sediments could escape the sand trap and be transported to the turbines. The simulations of stationary flow were performed with both Reynold Averaged Navier-Stokes (RANS) models and as a Detached Eddy Simulation (DES), using Star-CCM+ software. The geometry was built using geometry data from a laser scan, in order to capture all geometry details. Numerical results were compared to field measurements and showed good results with respect to both flow field representation and

sediment transport. It was found that the RANS simulations provided good results in regions with low level of turbulence, but DES is needed to capture the turbulent regions [5].

Roughness Modelling

The analyses of laser scanned geometries makes it possible to include the effect of the blasted rough walls of hydropower waterways. However, this approach requires a very fine mesh in order to capture the roughness elements and resolve the boundary layer. Additionally, it would require a shutdown of the hydropower system in order to empty the tunnels and perform the laser scanning. This leads to loss of income, which is not desirable.

There has also been performed research on how to link measured roughness of blasted tunnels to the hydraulic roughness [1, 6, 19]. This is helpful in order to analyse waterway designs without the requirement of tunnel scans. The roughness can then be added to the model artificially. Most commercial CFD codes have implemented rough wall models similar to the one developed by Launder and Spalding [15]. Unfortunately, these do not apply to large scale roughness, such as in blasted tunnels. This will be described in detail in the CFD theory chapter.

Instead of analysing a geometrically rough surface, Olsen and Stokseth [17] investigated the opportunity of applying a porosity model to model the roughness elements near the bed in a river flow. Using Navier-Stokes, the interaction between the porous and non-porous regions was investigated. The numerical flow field compared well to the velocity field measurements of the river Sokna [17].

Sediment Transport

The sediment transport in hydropower waterways can be modelled in several ways. The two most common models for handling solid-liquid multiphase are the Eulerian-Eulerian approach and the Eulerian-Lagrangian approach. In the Eulerian-Eulerian approach, the Navier-Stokes equations are solved for both phases and models are applied for how they interact. Research show that the Euler-Euler approach show good results for large particle concentrations [4, 9]. In the Eulerian-Lagrangian approach, the fluid phase is modelled as continuous using an Eulerian approach, and the solid phase is modelled discrete using a Lagrangian approach. As the particles can be released on an already solved flow field, the computational effort is smaller than for the Eulerian-Eulerian approach. Research performed by this approach show promising

results regarding simulating suspended particle transport through hydraulic structures, but the model was not able to give a realistic picture of the sediment movement near the bed [13, 23].

Automation of CFD Analyses

Automation of CFD analyses is widely applied in industry. Parametrisation of the analyses makes it possible to analyse several designs with the same CFD codes. However, this is often limited to smaller projects and used internally within the company. According to the author's knowledge, web-based CFD applications do not exist.

3 Theory

3.1 A Hydropower Plant

The main principle of a hydropower plant is to convert the potential energy of elevated water into electrical energy. This is done by leading the water through channels and pipes down to the turbines in the power plant. In the channels and pipes, the overlying water builds up a big pressure. This high-pressurised water runs the turbines and generates electricity. Figure 3.1 shows a principal sketch of a hydropower system [11].

As can be seen in Figure 3.1 the water might have to be led over a quite long distance before the power production can take place in the turbines. The aim is to transfer the water from the high altitude location and down to the power station without losing its energy. The vertical distance from the reservoir to the power plant is referred to as *total head*. On its way through the waterways, the water will always lose some of its energy due to for instance friction. This loss, often called *head loss*, is measured in meters and represents the equivalent column height of water. Hydropower plants can also be built in rivers with low total head, but with high mass flow. In such situation the plants are built more compact as can be seen in Figure 3.2.

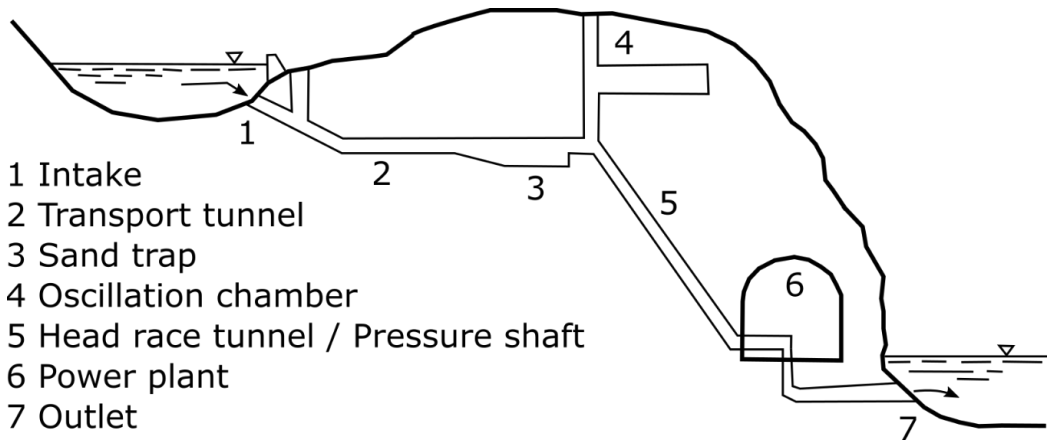


Figure 3.1 Principal sketch of a hydropower plant. Inspired by Eie [11].

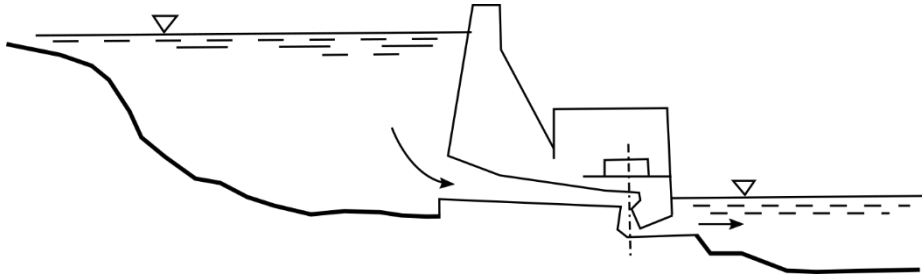


Figure 3.2 Low head hydropower plant [11].

Waterways

The waterways constitutes the veins in a hydropower system. The transportation of the water must be done without losing too much of the energy. High velocity is related to high friction losses, hence the tunnels are often built with big cross sectional areas, to obtain low velocity for given mass flow rates. On the other hand, bigger cross sectional area gives higher cost related to the excavation of rock. A circular cross sectional shape will provide the smallest contact surface between the water and the solid, but as large vehicles are used to transport workers, equipment and rocks when the tunnels are built, the tunnels are built with a flat bottom and high vertical walls. The ceiling is arced as this provides stability in the rock and favourable flow conditions [11]. A typical cross section of a hydropower tunnel can be seen in Figure 3.3. However, when the tunnels are long and straight, the use of *Tunnel Boring Machines* (TBM) becomes favourable. The TBM drills out the tunnel and provides a circular and relatively smooth cross section.

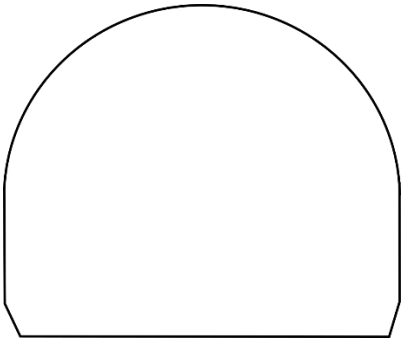


Figure 3.3 Typical cross sectional shape of a blasted hydropower tunnel [11].

The pressure shaft is a critical part of the waterways system. Here the water is transported almost vertically towards the power station and the pressure that builds up is extensive. Nowadays, the pressure shaft tunnels are normally blasted unlined tunnels, but in places with unstable rock formations, the water can be led into steel pipes casted in concrete [11].

The tunnels is most commonly blasted and unlined as this is the most cost efficient solution. The “gravel roads” that the vehicles drive on when building the tunnel is also left behind due to cost efficiency. These loose particles are desired to stay in rest at the tunnel floor, but can under the right flow conditions, for instance when the waterway system is filled up after a shut down, be carried all the way to the turbines. This could damage the turbines and could be expensive to repair. In addition sediments from the reservoir can be carried into the waterways. Therefore, sand traps are built inside the tunnels, often at the end of the transportation tunnel before the pressure shaft. See Figure 3.1. A sand trap is in principle just an expansion in the tunnel cross section that lowers the flow velocity, so that the sediments being transported by the flow falls to rest. A closer view of the sand trap can be seen in Figure 3.4. Turbulence and undeveloped flow conditions makes it recommended to place sand traps quite a long distance downstream of corners and similar. Over time the sand trap will be filled up, and needs to be cleaned out. This can be done by shutting down the plant and removing the gravel with an excavator. The vertical tunnel in the top right of Figure 3.4 is an oscillation chamber. It dampens the pressure oscillations that may occur in the system when for instance the turbine load changes rapidly [11].

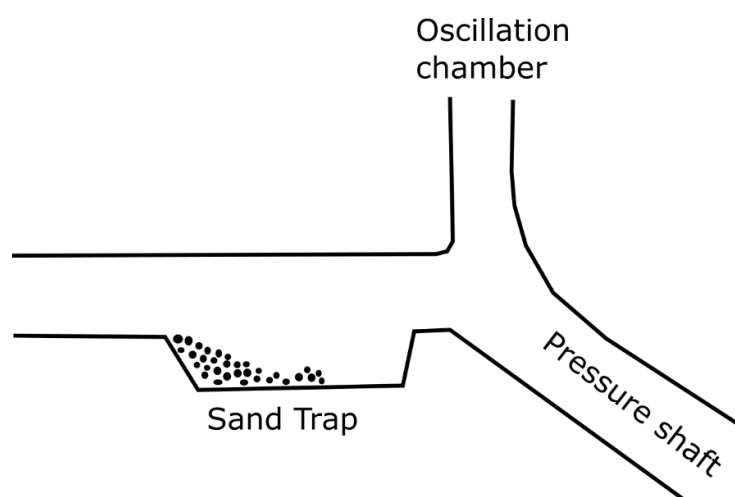


Figure 3.4 Principal sketch of a sand trap [11].

3.2 Internal Flow

In hydropower tunnels the flow can in many cases be classified as internal. This applies when the fluid fills the conduit completely and the flow is driven by primarily by pressure difference [7]. There are also situations, such as horizontal transport tunnels, where the flow in hydropower systems involves free surface flows and the flow is only gravity driven.

In hydropower systems the pressure in the tunnels and penstock is directly related to the output from the turbines. Hence, causes of pressure drop through the waterways is of great interest when dealing with hydropower. Friction is a major cause of pressure drop and is therefore important to pay attention to. Pressure drop can also occur when the flow pattern undergoes changes such as intersections, contractions or bends. These losses are often called minor losses or singular losses. By expressing the pressure loss in terms of the equivalent fluid column height, $h_l = \Delta P / \rho g$, the pressure loss can easily be related to the elevation of the reservoir.

The waterway analysis can in many cases be treated as a one-dimensional system. By looking at the flow along a stream line between the inlet and the outlet, the Bernoulli equation can be applied as an approximate for the relationship between pressure, velocity and elevation. By including a term for the head loss, we get what is known as the *energy equation*. Written in terms of heads, the difference in pressure, velocity and elevation at two points can be expressed as in Equation 3.1 below. The term h_L refers to the head loss due to friction or changes in the flow conditions [7].

$$\frac{P_1}{\rho g} + \frac{V_1^2}{2g} + z_1 = \frac{P_2}{\rho g} + \frac{V_2^2}{2g} + z_2 + h_L \quad 3.1$$

Friction Losses

Flow through closed conduits and pipes is widely applied in different industries and is quite well understood. However, analytical solutions is only possible for simple problems, hence, empirical knowledge is required when analysing internal flow for practical applications. Equation 3.2 shows the pressure loss in terms of head loss for a fully developed pipe flow. f is the Darcy-Weisbach friction factor, L is the length of the pipe, V is the velocity, g is the acceleration of gravity and D_H is the hydraulic diameter of the pipe. The hydraulic diameter is calculated using the cross sectional area, A_c , and the wetted perimeter, P_w . See Equation 3.3.

For pipes the hydraulic diameter is equal to the regular pipe diameter. For a horizontal pipe with constant cross section the pressure drop can be calculated with Equation 3.4 [7].

$$h_f = f \frac{LV^2}{D_H 2g} \quad 3.2$$

$$D_H = \frac{4A_c}{P_w} \quad 3.3$$

$$\Delta P = \rho g h_f \quad 3.4$$

The friction factor f is found using a Moody chart or the Colebrook equation from which the Moody chart is based on. Equation 3.5 shows the Colebrook equation and is valid for turbulent flow in smooth or rough pipes. However, it is important to be aware of the uncertainties related to the Colebrook equation, and thus the Moody chart as well. Usually, it is said to be accurate within $\pm 15\%$ [7]. In the Colebrook equation, ϵ is the roughness height, and Re is the Reynolds number of the pipe flow.

$$\frac{1}{\sqrt{f}} \cong -2.0 \log \left[\left(\frac{\epsilon/D_H}{3.7} + \frac{2.51}{Re\sqrt{f}} \right) \right] \quad 3.5$$

For water tunnels the Manning formula, Equation 3.6, together with the Manning number is used to find the head loss due to friction [11]. Where L is the length of the channel, V is the velocity of the flow, M is the Manning number, typically between 32 and 37 for blasted unlined tunnels [11]. R_H refers to the hydraulic radius, Equation 3.7. The link between Darcy friction factor and Manning constant is given in Equation 3.8 [18].

$$h_f = \frac{LV^2}{M^2 R_H^{\frac{3}{4}}} \quad 3.6$$

$$R_H = \frac{A_c}{P_w} \quad 3.7$$

$$f = \frac{8g}{M^2 R_H^{1/3}} \quad 3.8$$

Minor Losses

Sudden changes in the flow also contributes to head loss. These are called minor losses or singular losses and is present when for instance there is a narrowing of the channel, transition from channel to pipe, pipe bends and similar [7].

$$h_s = k \cdot \frac{V^2}{2g} \quad 3.9$$

The constant, k , is called the loss coefficient for a component and is decided by the geometry of the component. Values for k can be found in tables for various component geometries. Head loss coefficients for a selection of components are given in Appendix B. As with the friction losses, there are uncertainties related to the loss coefficients listed. As small variation in design can have significant impact on the pressure loss, the answers obtained by the given formulas coefficients, should not be treated as exact.

3.3 Sediment Transport

In hydropower systems, sand and small stones can be transported with the flow through the waterways. This sediment transport can be divided into suspended and bedload transport. Suspended load is the transport of smaller particles that are carried with the flow and almost never hitting the bottom. Bedload is bigger particles that slides, bounces and rolls along the bottom of the tunnel. The size of the particles transported is dependent on the flow conditions [21].

There are several methods to predict the sediment particle size transported by a flow. One of them applies the shear stress on the bottom to decide whether a particle will be eroded or not. If the shear stress exceeds the critical value, τ_c , stones and sand will be eroded. This critical

shear stress is dependent on the size and density of the particle to be eroded, together with the density, viscosity and velocity of the fluid. The critical shear stress for erosion of particles on a flat bed is formulated as in Equation 3.10. Where C_s is the Shield's number, ρ_s and ρ is the density of the particle and fluid respectively, and D_p is the diameter of the particle [21].

$$\tau_c = C_s g (\rho_s - \rho) D_p \quad 3.10$$

The velocity field near the bed can be expressed using Keulegan's formula in Equation 3.11. $u(z)$ is the velocity of the water in height z above the bottom, u_* is the shear velocity and k_s is the roughness height of the bottom surface. Further, the shear force at the bed can be expressed as in Equation 3.12. The Shield's diagram, in Figure 3.5, relates the Reynolds number in the boundary layer to the shields number. The boundary layer Reynolds number is given in Equation 3.13 below, where ν is the kinematic viscosity of the fluid [21].

$$\frac{u(z)}{u_*} = 5.75 \cdot \log_{10} \left(\frac{30.2 \cdot z}{k_s} \right) \quad 3.11$$

$$\tau = u_*^2 \cdot \rho \quad 3.12$$

$$Re_* = \frac{u_* \cdot D}{\nu} \quad 3.13$$

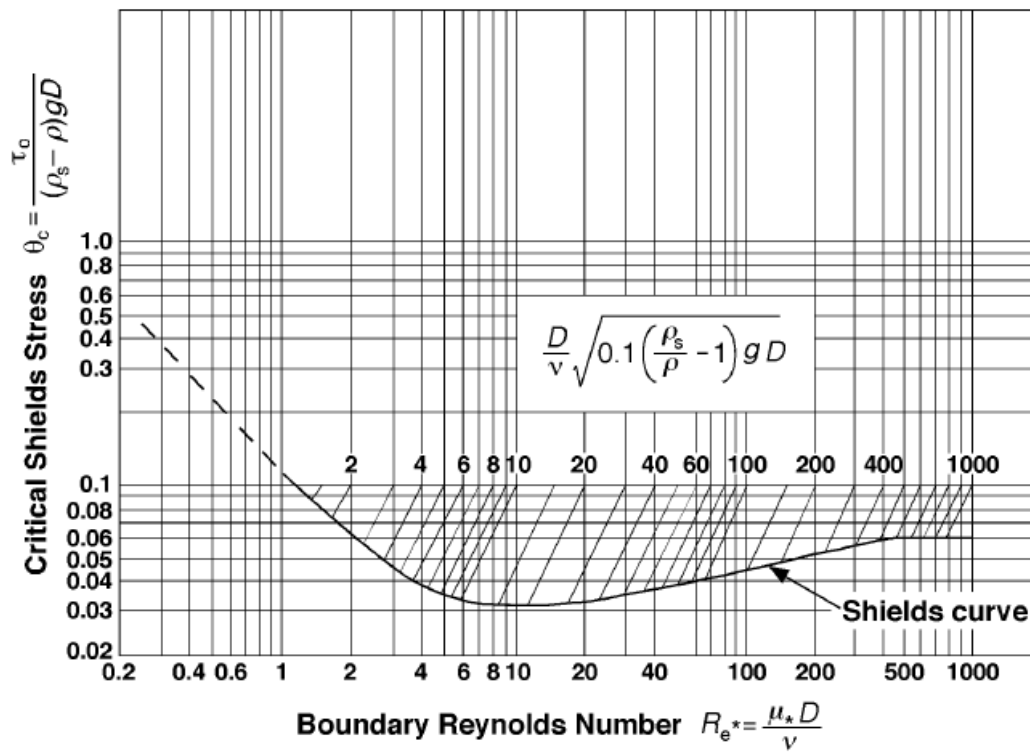


Figure 3.5 Shield's diagram for movement of bottom particles [20].

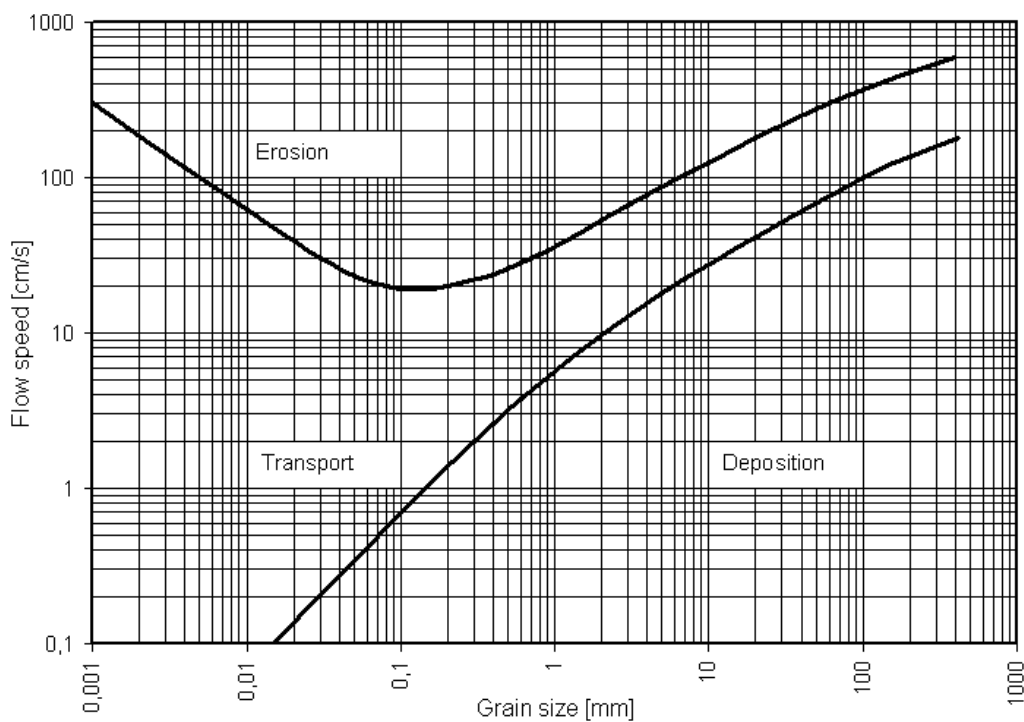


Figure 3.6 Hjulström's diagram for deposition, transport and erosion of particles [21].

Another parameter that can be used to determine transport of particles is the mean velocity of the flow. Hjulström's diagram, in Figure 3.6, depicts the velocity needed for particles of varying sizes to be in rest, suspended or eroded [21]. In general, the diagram shows that the bigger particle, the higher velocity is required to erode the particle. Erosion of particles is when the particles are starting to move either by suspension or bedload transport. The part to the left on the diagram, where the erosion velocity curve is decreasing for increasing diameter is due to mud creation that requires higher velocities to erode. When the particles are above a certain size, this mud creation does not occur. The diagram was made for free surface flows and the average velocity of the flow. However, it has been shown that it also provides good estimates for sediment transport in closed conduits [18].

So far, the theory presented on sediment theory is based on free surface flow. Equation 3.14 determines the critical diameter of particle erosion in internal flow [5]. U is the average velocity of the fluid and C_p is an empirical constant found to be in the range of 115 to 140. A is the cross sectional area of the tunnel.

$$D_c = \frac{\rho}{\rho_s - \rho} \cdot \frac{U^2}{C_p \cdot A^{1/6}} \quad 3.14$$

3.4 Roughness Estimation

The estimation of roughness in blasted tunnels can be done by the application of the IBA method [19]. This statistical method uses cross section and wall measurement data from a laser scan of the tunnel to calculate the total roughness. This way the friction factor and theoretical head loss of the tunnel can be found by the Equations 3.2 and 3.5. The method is also useful in order to model an artificial rough surface based on field measurements of head loss. Figure 3.7 and the Equations 3.15 - 3.19 describes the method.

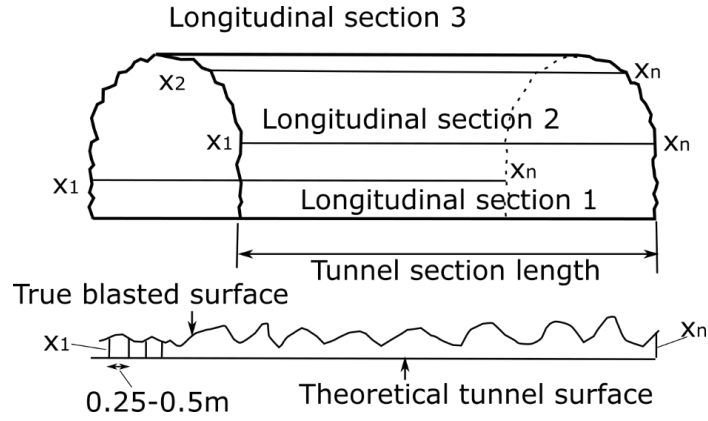


Figure 3.7 Tunnel roughness estimation by the IBA method [19].

$$Total\ roughness = k_s = rms_{wall} + rms_{cross\ section} \quad 3.15$$

$$rms_i = \sqrt{\sum_{i=1}^n \frac{(x_i - \bar{x})^2}{n}} \quad 3.16$$

$$rms_{wall} = \sqrt{\sum_{i=1}^m \frac{(rms_i)^2}{m}} \quad 3.17$$

$$rms_j = \sqrt{\sum_{i=1}^n \frac{(A_i^{0,5} - \bar{A}^{0,5})^2}{n}} \quad 3.18$$

$$rms_{cross\ section} = \sqrt{\sum_{i=1}^m \frac{(rms_j)^2}{m}} \quad 3.19$$

4 CFD Theory and ANSYS CFX

Computational Fluid Dynamics (CFD) is a powerful tool when analysing fluid flow problems. In order to solve even simple flow problems analytically, the Navier-Stokes equations must be simplified significantly. To avoid this simplification a numerical approach is required. The flow problem can then be solved iteratively on a computer and more complex flow problems can be analysed. With the development of both computer hardware and CFD software seen in the past decades, CFD has become an important tool for engineering and research applications.

In CFD analyses, the computational domain, i.e. the region to be analysed, is divided into a grid of small cells, often referred to as *mesh*. Physical variables, such as velocity, pressure and temperature are stored at nodes inside or at the vertices of the cells. See Figure 4.1. This discretisation turns the differential equations of motion into a system of algebraic equations that can be solved on a computer [24].

Definition of fluid properties, setting appropriate boundary conditions and selecting the phenomena to be observed is done in a Pre-Processor. After this the flow problem can be analysed in a Solver. Here the algebraic equations are solved iteratively. When the solution has reached a predefined level of convergence, or maximum computational time, the results can be analysed in a Post-Processor. Numerous visualisations of physical properties can be obtained, such as colourful contour plots, 3D volume renderings and particle tracking [24].

The software chosen for this project is the commercial code ANSYS CFX 17.0. CFX is a control volume based solver that uses finite elements to discretise the domain. As the CFX solver is vertex centred, the variables are stored at the cell vertices. A visualisation of this is given in Figure 4.1[3].

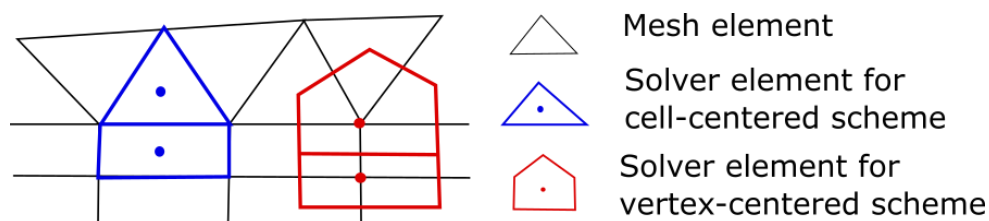


Figure 4.1 Cell centered and vertex centered numerics [2].

The governing equations of ANSYS CFX are the Conservation of mass (Continuity equation) and Conservation of Momentum (Navier-Stokes equations). Assuming incompressible flow and ignoring gravity we get the Equations 4.1 and 4.2. CFX also solves Conservation of Energy for thermal studies, but this is not performed in this Master's work [3].

$$\frac{\partial u_i}{\partial x_i} = 0 \quad 4.1$$

$$\rho \frac{\partial u_i}{\partial t} + \rho \frac{\partial u_i u_j}{\partial x_j} = -\frac{\partial p}{\partial x_i} + \mu \frac{\partial^2 u_i}{\partial x_j^2} \quad 4.2$$

4.1 Meshing

With the solution to the flow problem stored at the nodes, the accuracy of the solution depends on the number of nodes. More nodes gives a more accurate solution, but at the price of extra computational cost. Because of this, it is important to find an acceptable balance between desired accuracy of the solution and available computational resources. The mesh quality does also have great influence on the accuracy of the solution. Complex areas such as sharp edges and small faces are often associated with bad quality elements and collapse of the cells in the mesh. It is desired that the elements are not too distorted, stretched and differs in size compared to adjacent elements. A list of the quality measures used in the ANSYS CFX Solver can be seen in Table 4.1. Figure 4.3 describes the mesh quality measures figuratively.

The cells in the mesh can have various shapes. The choice of shape is dependent on geometry of the model, flow conditions, required accuracy and available resources. Figure 4.2 depicts the different shapes available in ANSYS Meshing. As CFX is a vertex-based solver, the use of Tetrahedral elements gives more iterations due to increased interpolation with neighbouring nodes. Use of *hexahedral* element gives a nice uniform mesh and it usually provides a faster solution. This is true because hexahedral elements normally provides better quality and because the number of interpolation surfaces decreases. However, in complex geometries, the generation of a non-uniform mesh with *tetrahedral* elements can be done with a high degree of automation.

Table 4.1 ANSYS CFX Mesh quality measures [2].

Mesh quality measure	Acceptable range	Description
Orthogonal angle	$> 20^\circ$	How close the angles between adjacent element faces of adjacent element edges are to some optimal angle (90° for quadrilaterals and 60° for triangular faces). See Figure 4.3.
Expansion factor	< 20	Rate of change of magnitude of adjacent element face area or volumes. See Figure 4.3
Aspect ratio	< 100	How stretched the mesh elements are. See Figure 4.3.

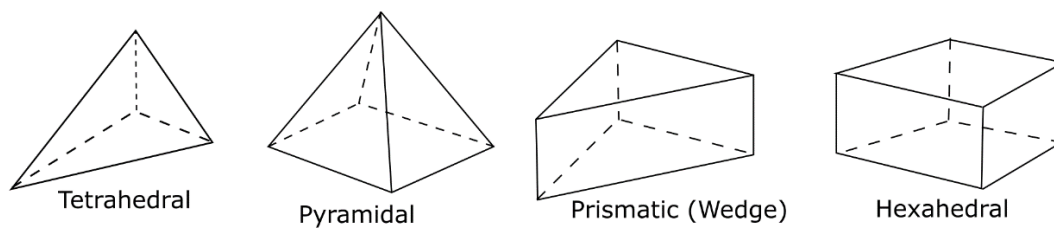


Figure 4.2 Mesh element shapes in ANSYS CFX [2].

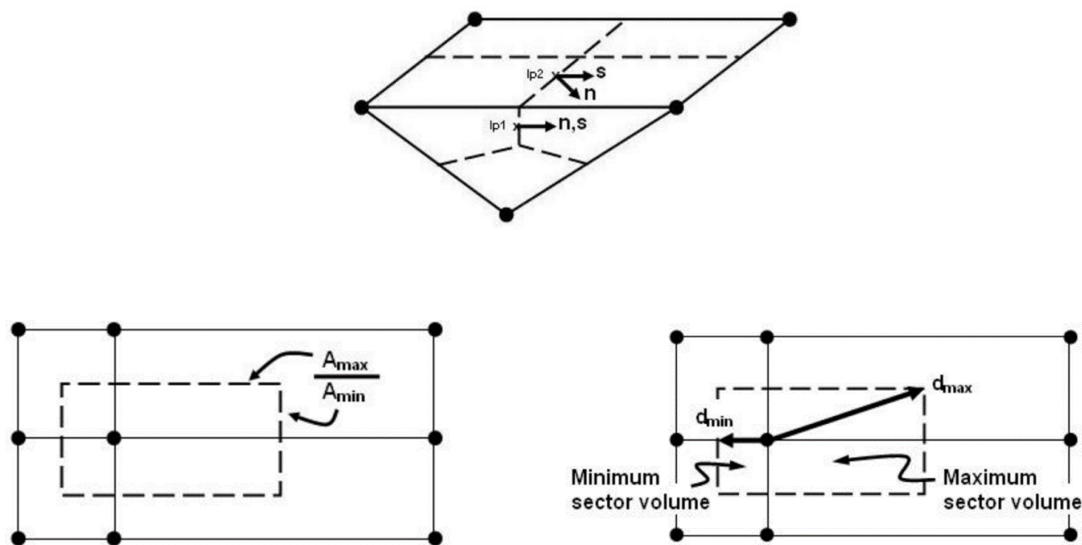


Figure 4.3 Overview of the ANSYS CFX mesh quality measures [3]. Orthogonal angle (top), Aspect ratio (bottom left) and Expansion factor (bottom right)[2].

4.2 Turbulence

When turbulence is present, the velocity in one single point can be very different from the next point. The fluctuating velocities makes it difficult to solve the equations of motion. There are several approaches to coping with turbulence and the most accurate are *Direct Numerical Simulations* (DNS). DNS solves Navier Stokes directly, hence simple problems get complicated to solve. Another approach is the *Large Eddy Simulations* (LES). LES simplifies the problem by spatial low-pass filtering of the turbulent vortices. The eddies that are bigger than a certain size are simulated, while models are applied in order to represent the smaller eddies. This reduces the computational cost, but the LES require transient analyses and is still very time consuming [24].

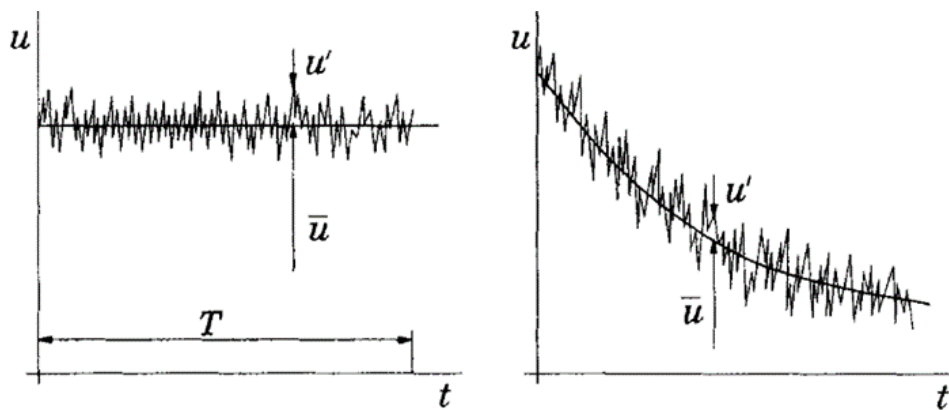


Figure 4.4 Turbulence time averaging for a statistically steady flow (left) and ensemble averaging for an unsteady flow (right) [12].

A very common approach, and less time consuming than the previous mentioned methods, is the *Reynolds-Averaged Navier Stokes equations* (RANS). They have shown to be a good compromise between computing time and accuracy, as average effects and the development of the turbulence often is of interest, rather than the turbulent structures itself. In the RANS method, the pressure and velocity are averaged in time, as shown in Figure 4.4. This provides the expression $u = \bar{u} + u'$, where u' is the fluctuating velocity component. The same is done to the pressure and put into the Navier-Stokes Equations. What comes out on the other side is the Reynolds-Averaged Navier-Stokes Equations [24].

$$\rho \frac{\partial \bar{u}_i}{\partial t} + \rho \frac{\partial \bar{u}_i \bar{u}_j}{\partial x_j} = -\frac{\partial \bar{p}}{\partial x_i} + \mu \frac{\partial^2 \bar{u}_i}{\partial x_j^2} - \frac{\partial}{\partial x_j} (\rho \overline{u'_i u'_j}) \quad 4.3$$

The last term on the right hand side of the RANS equations is called the Reynold Stress term. The term is a symmetric 3x3 tensor that adds a set of 6 unknowns to the Navier Stokes equations. That leaves us with a set of 4 equations and 10 unknowns, often referred to as the closure problem. In order to solve the system we need models. Boussinesq approximations introduces a relation between the Reynold stress and eddy viscosity. This reduces the six unknown to only two, which can be modelled with turbulence models. There are several models available, such as the $k - \epsilon$ and $k - \omega$ model. They are classified as so-called two equation models, as they provide two additional transport equations for the solver to calculate. In the $k - \epsilon$ model the turbulent kinetic energy and the rate of turbulent dissipation is the transported variables. The $k - \omega$ model regards the transport of turbulent kinetic energy and turbulent frequency [24].

In this master's work a different model is preferred, the *Shear Stress Transport (SST)* model. It is a hybrid model that takes advantages of the strengths and leaves out the weaknesses of the $k - \epsilon$ and $k - \omega$. The $k - \epsilon$ shows good performance in the free stream, but gives poor results in near-wall regions. The $k - \omega$ shows the opposite trends, good performance in near-wall regions and unsatisfactory results in the free stream. In the SST model the $k - \omega$ is used in the near-wall regions and the $k - \epsilon$ is used in the fully developed turbulent regions in the free stream. Blending functions are used to achieve a smooth transition between the two models. An extra term for the transport of shear stress is also added to the system, which explains the name of the model [24].

4.3 Pressure Representation in ANSYS CFX

In this master's work the *Total Pressure* is used as variable of interest when it comes to convergence. The total pressure is in ANSYS CFX defined as the sum of the static and the dynamic energy in the flow. See Equation 4.4. Gravity of the flow is often not included in simple flow analyses, and the pressure difference between the inlet and the outlet defines the development of the flow. Hence the elevation components (z_1 and z_2) of the energy equation is left out of the equation. For incompressible flows, the energy equation in terms of total pressure reduces to Equation 4.5 [3].

$$P_{tot} = P_{stat} + \frac{V^2 \rho}{2} \quad 4.4$$

$$P_{tot,1} = P_{tot,2} + h_L \rho g \quad 4.5$$

4.4 Wall Functions

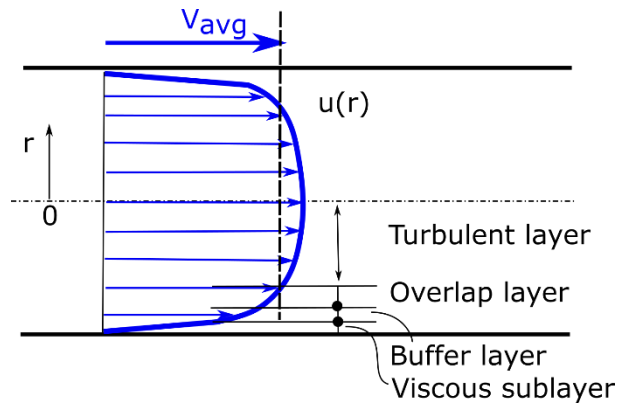


Figure 4.5 Turbulence velocity profile [7].

In turbulent flows the velocity gradient near the wall can be divided in four regions. Close to the wall, you find the viscous sublayer where the viscous effects are dominant. Here, the velocity profile is almost linear. The next region is the buffer layer. This is a transitional zone where the turbulent effects become more significant, but the flow is still dominated by viscous effects. Further out is the overlap layer, in which the turbulent effects are even more significant, but not dominating the viscous effects. The last region is called the turbulent layer, in which the turbulent effects are dominating the viscous effects [7].

The non dimensional parameter y^+ is introduced to describe the distance from the wall [7]:

$$y^+ = \frac{\rho \Delta y u_\tau}{\mu} \quad 4.6$$

Here, the friction velocity, u_τ , is defined as the root of the wall shear stress, τ_ω , divided by the fluid density ρ [7]:

$$u_\tau = \left(\frac{\tau_\omega}{\rho} \right)^{\frac{1}{2}} \quad 4.7$$

In the viscous sublayer, the velocity profile is expressed in dimensionless form as:

$$\frac{u}{u_\tau} = \frac{\rho y u_\tau}{\mu} \rightarrow u^+ = y^+ \quad 4.8$$

The thickness of the viscous sublayer is found to be approximately $0 \leq y^+ \leq 5$. In the overlap layer, which is found to be when $y^+ > 30$, the velocity profile can be expressed as:

$$u^+ = \frac{U_t}{u_\tau} = \frac{1}{\kappa} \ln(y^+) + B \quad 4.9$$

Here, u^+ is the near wall velocity, U_t is the known velocity tangent to the wall at a distance of Δy from the wall. y^+ is the dimensionless distance from the wall, τ_ω is the wall shear stress, κ is the von Karmans constant, and B is a log-layer constant depending on wall roughness [7].

When using the SST model for turbulence in ANSYS CFX, automatic wall functions are applied when modelling flow near walls. If the first node of the mesh is located outside the boundary layer, that is for high values of y^+ , the wall function will be used. For lower values of y^+ , when there are nodes within the boundary layer, the values calculated by the solver is used. So, in order to take advantage of $k - \omega$ in the near wall region, a $y^+ = 2$ is required with at least 10 nodes within the boundary layer [2].

4.5 Rough Wall Modelling in CFD

There are several ways to analyse rough surfaces in ANSYS CFX. The main approaches are shown in Figure 4.6. The first one is by simulating the actual roughness elements, using a very fine mesh in order to resolve the geometrical shape of the roughness elements. A too coarse mesh will cut the edges, and even out the roughness elements. This approach is used when analysing laser scanned geometries, such as Brevik's analyses of Tonstad Hydropower station [5]. The requirements of the mesh related to this type of analyses leads to high computational cost.

The easiest way to account for the roughness, from a user’s perspective, is to apply the CFX model for treatment of rough walls. As wall roughness increases the wall shear stress and distorts the viscous sublayer, a downward shift is performed to the logarithmic velocity profile near the wall. The magnitude of the shift is decided by the roughness height. Figure 4.7 shows this downward shift figuratively. However, as the wall laws only apply to the first cell near the wall, the model is not applicable when the height of the roughness elements are in the same magnitude as the distance to the first cell [3]. In those situations a porosity model can be added to the cells near the wall instead. This approach was proposed by Olsen and Stokseth [17], and seem to give reasonable results compared to field measurements in the Sokna river.

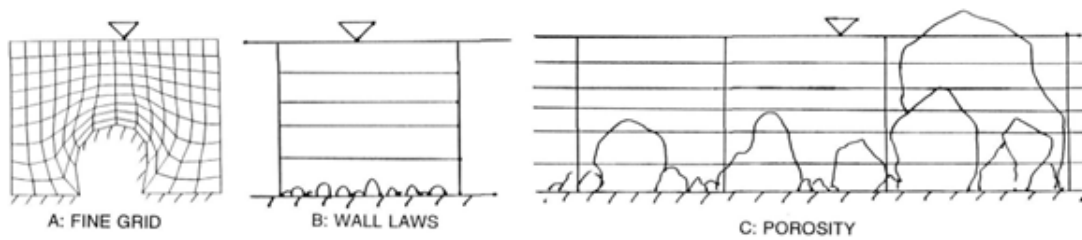


Figure 4.6 Different approaches to the rough wall modelling in CFD applications [17].

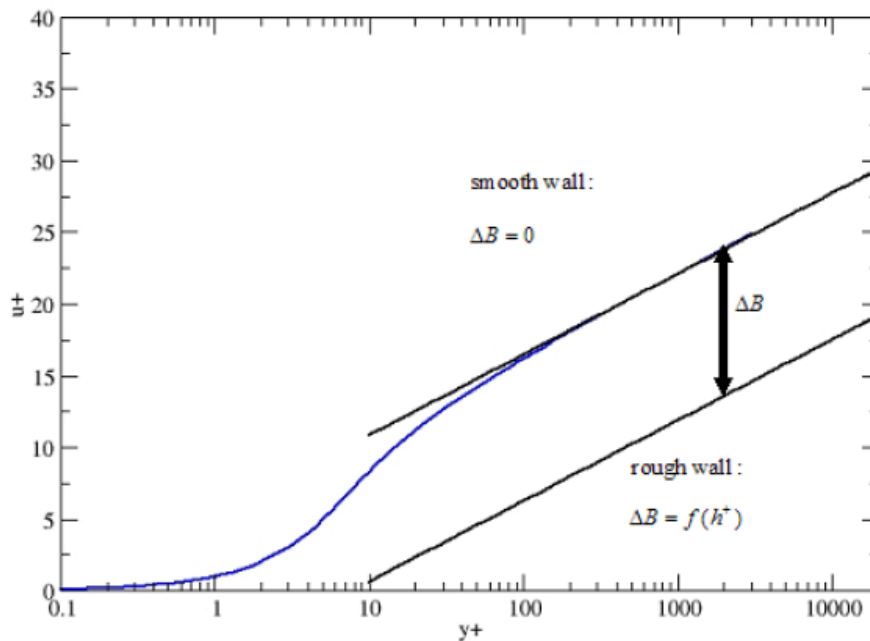


Figure 4.7 Downward shift of the Logarithmic Velocity Profile in ANSYS CFX [2].

4.6 Particle Tracking in ANSYS CFX

When particles such as stones and sand are added to the simulations, the flow becomes multiphase. The solid-liquid multiphase can be modelled in several ways. The most common models are the Eulerian-Eulerian and the Eulerian-Lagrangian approach. In the Eulerian-Eulerian model, the sediments are considered as a continuous phase and a volume fractions of the solid and the liquid are calculated in each cell. As this approach will not be applied in this master's work, further details of the Eulerian-Eulerian model can be found in the ANSYS CFX Solver Modelling Guide [2].

The Eulerian-Lagrangian is the second approach and is the approach chosen for this study. Here, the particles are modelled discretely distributed in a continuous phase. The continuous phase, water in the hydropower case, is solved using an Eulerian transport model, while the particles are solved using a Lagrangian transport model. The liquid-solid interaction can be set to be both one-way coupled and two-way coupled. In the one way coupling the fluid interacts with the particles, but the particles does not affect the fluid. For smaller concentrations of particles, the one way coupling is desired as it minimises the computational costs [2].

The forces acting on the particle are the viscous drag force, buoyancy forces, virtual mass and pressure gradient forces. The sum of these forces decides the trajectories of the particle. The amount of particles that have travelled all the way to the outlet is given as output in the simulation. If the forces acting on the particle are too low to keep the particle in motion, the particle will fall to rest inside the domain. By releasing a relatively high number of particles on the inlet, the statistical probability that a particle of a certain diameter will make it to the outlet can be found [2].

A third option to the multiphase simulations is the Algebraic Slip Method. Here, the momentum equations is solved only for the main fluid. This is a simplification of the traditional Eulerian multiphase models and is applicable when non drag forces are not significant and when the dispersed phase reach terminal velocity quickly. Hence, the model is inappropriate when the particles are above a certain size. Additionally, the particles interaction with the walls are difficult to implement in the Algebraic Slip Method. An opportunity is to include a wall deposition function, but this makes the particle phase disappear when it touches a wall. Therefore, the resuspension and erosion of particles is not possible [2].

4.7 Errors and Uncertainties in CFD

The application of CFD analysis can save both time and money in many situations. Expensive manufacturing of prototypes for experiments, hours paying salary to laboratory workers and time consuming experiments could be replaced or at least limited by one worker with a computer. In addition, a large number of simulations could be conducted in order to optimise designs. However, complex simulations can demand supercomputers with thousands of cores running for several days. Licences for the software can be very expensive and lastly but not least, the required knowledge of fluid dynamics to analyse and evaluate the result are substantial. With the commercial CFD codes available today it is not difficult to get a result and some nice colourful pictures from a simulation. The problem is that the results does not necessary represent the reality.

Big and costly decisions regarding design of different products are often based on results from CFD analyses. There are always a chance of errors or uncertainties in the numerical model, and to be aware of the potential deficiencies they can provide is extremely important. Deviation from real life can be caused by both user and the software. A list of potential errors and uncertainties is given in Table 4.2.

To cope with the vast amount of possible deficiencies the verification and validation processes is a vital part of the CFD analysis. The following definition is widely accepted [24]:

- **Verification:** *The process of determining that a model implementation accurately represents the developer's conceptual description of the model and the solution to the model.*
- **Validation:** *The process of determining the degree to which a model is an accurate representation of the real world from the perspective of the intended users of the model.*

The verification considers the effects of for instance mesh refinements and round off errors, while the validation compares the physical model to a real world solution that can be obtained from for instance experiments and empirical knowledge.

Table 4.2 Types of errors and uncertainties in CFD analyses [24].

Numerical errors:	
Round-off errors	Number of decimal points in the calculated values may have a significance on the accuracy.
Iteration errors	Deviations between converged solution and the solution at the iteration which the analysis was finished.
Discretisation errors	Refinement of the mesh yields significantly different results. When the solution is not mesh independent.
Coding errors:	
Software error	Bugs in the software
User errors:	
Human error	Incorrect use of software
Input uncertainty:	
Domain geometry	Over simplifications of the geometry may lead to deviations between real life scenario and the computed.
Boundary conditions	Misinterpretations in location and type of boundary conditions. Invalid assumptions such as temperature, velocity etc.
Fluid properties	Density, viscosity, thermal conductivity etc. depends on local values of the flow parameters. Assumptions of constant fluid properties may be wrong.
Physical model uncertainty:	
Accuracy and validity of submodels	Choice of submodels such as turbulence models, multiphase etc.
Oversimplifying assumptions	Assuming steady state, when flow really has transient effects. Assumptions of symmetry, incompressibility etc.

5 Automated CFD Application

The automated CFD application is supposed to be a web based service where the user can design a geometry consisting of several geometry components. The geometry components are chosen from a drop down menu and measurements are typed in as input. When all the geometry details are specified, the user are presented a preview of the geometry. If the geometry satisfies the requirements of the user, the job is submitted to a remote computer. Here, the geometry generation, meshing, setup and the execution of the analysis will take place automatically, without human interaction. As the end user of the automated CFD solver application will be able to choose from a range of geometries, the analyses will vary significantly in complexity. In order to rely on the results of such an analysis, the solver must provide acceptable results every time. To achieve this several combinations of the geometry components will have to be tested thoroughly. The testing will include studies of requirements related to mesh resolution, roughness modelling, sediment transport and how to use pressure as inlet input parameter. After an initial validation of the CFX solver, the following chapters will address the four topics separately. All the chapters will include descriptions of the analyses' geometry, meshing and setup, followed by results and a discussion. The findings in the four chapters will be applied when validating the model against field measurements of Tonstad Hydropower station.

5.1 Initial Validation of the CFX Solver

Geometry, Meshing and Setup

In order to get an initial validation the CFD solutions, a simple pipe to pipe geometry with a sudden contraction was analysed. The geometry consisted of a 100 meter pipe connected to another pipe of equal length, but with a smaller cross sectional area. A picture of the geometry can be seen in Figure 5.1. Ansys DesignModeler was used to build the geometry by sketching the cross sectional areas at certain locations and using the function *Skin/Loft* to fill the volumes in between the sketches. Four meshes of increasing mesh density was created in Ansys Meshing in order to achieve a mesh independent solution. A mesh of tetrahedral elements was chosen, as this is robust and it is simple to implement in the automated CFD application. Good quality meshes was created using body sizing and applying an inflation layer at the wall of the pipes. With tetrahedral elements in the mesh, the inflation layer consists of prism shaped elements. Using *SST* model for turbulence the steady state analysis was performed in CFX. As pressure losses is an important quantity of interest in hydropower systems, the pressure drop from the inlet to the outlet of the pipe geometry was monitored and used as convergence criteria. The walls are modelled as smooth walls with no slip condition, meaning that the velocity at the wall is zero. As the geometry is relatively simple the results can be compared to hand calculations obtained using Equation 3.9 and the head loss coefficient for sudden contraction in Appendix B.

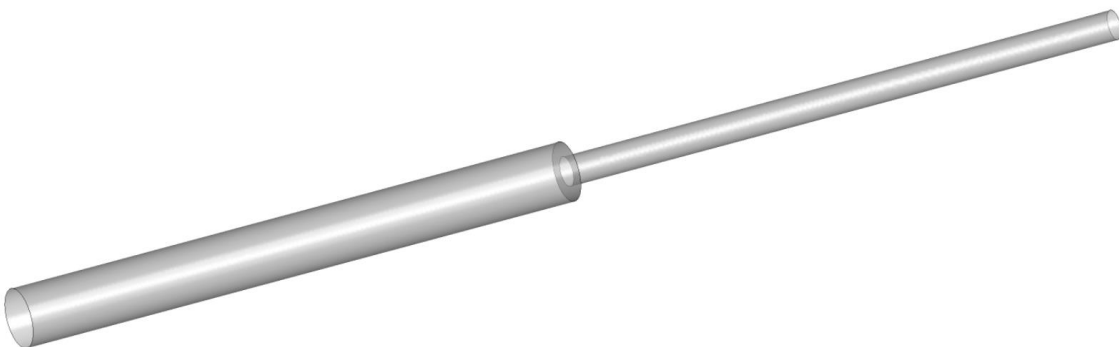


Figure 5.1 Geometry of the simple pipe-to-pipe connection used for initial validation.

Results and Discussion

Friction and geometry changes contributes to the pressure drop as the flow pass the domain. With increasing mesh resolution, the calculated pressure drop from the CFD solution seemed to converge towards the hand calculated pressure drop. Hence, the CFD model succeed in measuring the pressure drop for simple geometries. This way one can assume that more complex geometries, that are more difficult to analyse with hand calculations, also can be analysed properly with the use of CFD. The results are presented in Figure 5.2.

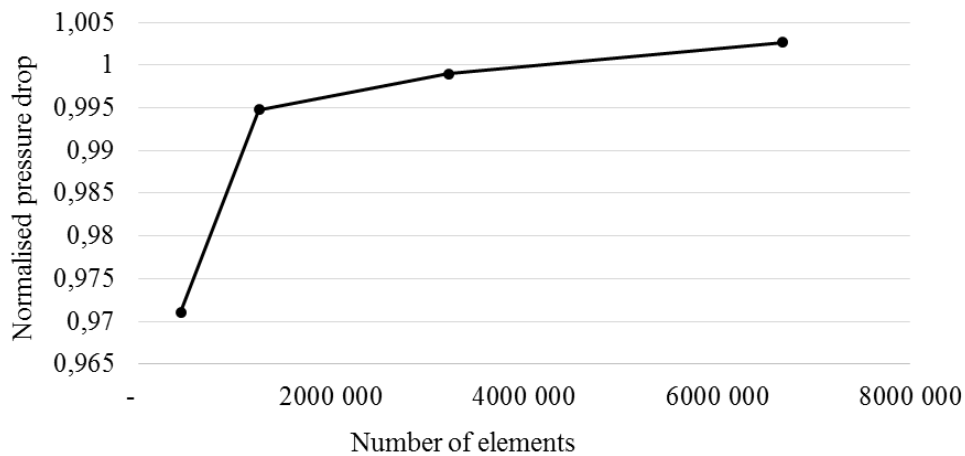


Figure 5.2 Study of a pipe-to-pipe connection with a sudden contraction. Pressure drop from inlet to outlet. The pressure drop is normalised to the solutions obtained from hand calculations.

6 Mesh Resolution Study

Mesh independence studies constitute for a great portion of the work done by the user in CFD analyses. The mesh have to be fine enough to provide reliable results, but at the same time be coarse enough to have an acceptable computational cost. The required number of elements varies significantly with the complexity of the geometry and flow conditions. However, as the mesh in the automated solver will have to be automatically generated, it is desired to find a rule of thumb for the mesh requirements. The goal was to do the meshing process as simple as possible in order to get a robust mesh generation in the automatic solver without human interaction. As the geometries can vary in both size and complexity, the required body size of the mesh elements used, might be different for each geometry. Therefore, the ratio between hydraulic diameter and required body size for a mesh independent solution is investigated for different geometries.

This chapter is divided in subsections that will cover the mesh resolution studies of a three different geometries. The geometries, which are typical for hydropower systems, were meshed with increasing mesh resolution in order to find a balance between accuracy and computational cost. Each subsection will include details on the geometry, mesh, setup and a presentation of the results. A summary and conclusion of the mesh resolution study are given at the end of the chapter, in Section 6.4.

6.1 Test Geometry 1 – Tunnel to Pipe

At first, a typical geometry found in hydropower systems was created using DesignModeler. The analyses of this geometry will from now on be referred to as *Test Geometry 1* or the abbreviated *TG1*. The geometry consisted of a tunnel section with a half sphere obstruction representing a downfall of rocks. The height of the tunnel was set to 1.5 meters. Further downstream the flow is going through a sudden contraction and continues into a pipe of diameter 0.5 meter. See Figure 6.1.

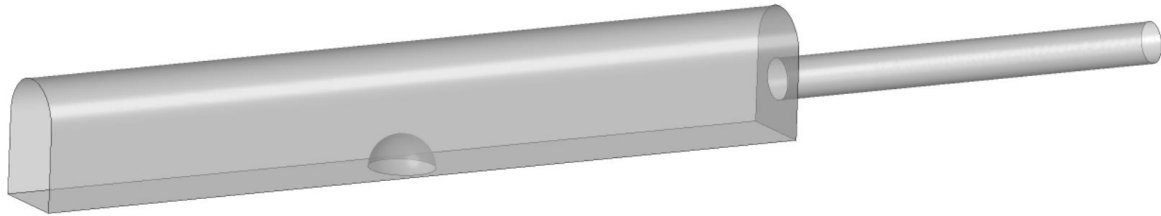


Figure 6.1 Test Geometry 1 – Tunnel to pipe geometry.

Mesh Resolution

Initially a quite coarse mesh specified with a body sizing and inflation layers was created. Due to the sudden contraction and the rockfall regions of increased mesh refinement was assumed necessary. This was controlled using the *Face size* function. The simulations was started with the aim of reaching a $y^+ < 2$. As described in the theory chapter on CFD, Section 4.4, this was done to capture the velocity gradients in the boundary layer. An initial value of y^+ was achieved by adjusting the First Layer Thickness in the inflation layer to match the calculated y^+ for tunnel flow using Equation 4.6. In the pipe the flow is subject to higher velocity, thus the first layer thickness have to be smaller in this region. Due to the contraction from tunnel to pipe, higher velocity regions occur and the first layer thickness was adjusted by trial and error to get a $y^+ < 2$ at all walls in the domain. When this was achieved, a mesh dependence test was performed by simulating the flow with increasing mesh density.

In order to test how round off errors affected the results, the simulations of the coarsest and the finest mesh was run one extra time with double precision option ticked off in the CFX solver input file. As described in the theory section, double precision includes more decimals in the calculations, hence the solution increases in accuracy. However, this also increase the computational time, and is often not required to obtain preferred level of accuracy in the solutions. The model was also checked for time dependent effects by running a transient simulation on the coarsest mesh. The transient simulations was initiated from the steady state results and was run until convergence in pressure drop from the inlet to the outlet was reached.

At the inlet a velocity of 0.5 m/s was specified. The outlet was set to be a pressure outlet with a value of 0 Pascal. The walls are modelled as smooth walls with no slip conditions.

Sensitivity of y^+

Another important aspect of the mesh dependency testing is the significance of y^+ . As a low value of y^+ is required to capture the near wall boundary layer a fine inflation layer will have to be added to the model. For an automated solver the tuning of y^+ can be difficult, and it is desired to check for y^+ dependency. The previous simulations showed that the model, with a $y^+ < 2$, was declared mesh independent at the coarsest mesh, approximately 3 million nodes. This mesh was used further in the y^+ investigations. By slowly increasing the first layer thickness of the 3 million nodes mesh, the distance to the first grid point, y^+ , was increased accordingly. The other parameters, body size and face size, was held constant.

Sensitivity to Mass Flow Rate

To see whether the requirements of the mesh resolution changes with the flow conditions, a mesh dependency test was run at two additional mass flow rates. The velocities on the two additional simulations was set to be 0.8 and 0.3 m/s. According to findings in the y^+ study, the y^+ was kept at a level between 100 and 300. The mesh details of the meshes used in the mass flow rate sensitivity studies are listed in Table 6.1. For later reference, the meshes are named according to the geometry and approximate number of cells. For example, TG1-3M is the mesh of Test Geometry 1 containing approximately 3 million cells.

Table 6.1 Mesh details of Test Geometry 1 – Sensitivity of mass flow rate study.

	TG1-1M	TG1-3M	TG1-6M
Body Size, whole domain [m]	4.50e-2	2.25e-2	1.50e-2
Face Size, regions of increased mesh density [m]	3.00e-2	1.50e-2	1.00e-2
First Layer Thickness, pipe [m]	2.00e-4	2.00e-4	2.00e-4
First Layer Thickness, tunnel [m]	8.00e-4	8.00e-4	8.00e-4
Inflation layer growth rate	1.15	1.15	1.15
Number of elements	887 934	3 612 959	6 600 000
Hydraulic diameter/Body size ratio in tunnel	27.1	54.2	81.3
Hydraulic diameter/Body size ratio in pipe	11.1	22.2	33.3

Results and Discussion of Test Geometry 1

Mesh Resolution

With a $y^+ < 2$, the model seemed to provide good results with all the investigated meshes. The results varied by just a little more than 1% from the coarsest to the finest mesh, which implies that the coarse mesh can be used and still provide acceptable results. The double precision did not seem to have significant effect on the result. The results are visualised in Figure 6.2.

With the coarsest mesh, consisting of 3 million nodes, providing results within 1% from the finest mesh, it is concluded that 3 million nodes is sufficient for this geometry under the specified flow conditions.

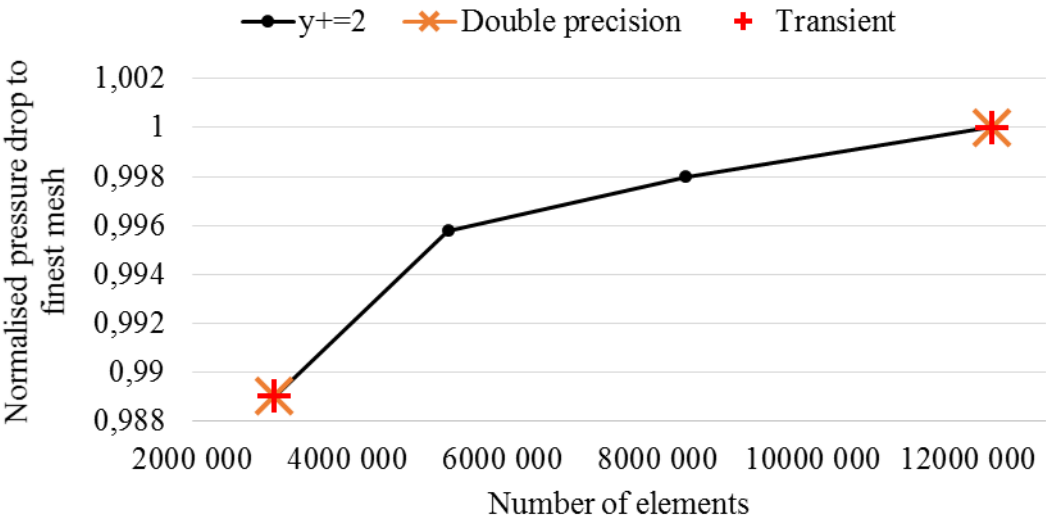


Figure 6.2 Mesh dependence test of Test Geometry 1. $y^+ < 2$ and the y-axis displays the pressure drop normalised to the mesh with the highest number of elements. The results from the runs with double precision is plotted with the orange crosses.

The pressure at the inlet was monitored during the simulations and used as convergence target for the simulations. As the outlet pressure was specified to be zero Pascal, the inlet pressure is equal to the pressure drop over the geometry. The monitors showed that the inlet pressure did not fully converge. Instead of gradually moving towards a steady state value, the pressure at the inlet fluctuated around some average value. This is a clear indication that the flow has transient effects. Especially for the finest meshes, these turbulent effects was captured better. These fluctuations are expected effects as the transition from duct to pipe involves a stagnation point

for the flow that will affect the steadiness of the pressure at the inlet. In order to see whether these transient effects had significant impact on the steady state results, the analyses was also run transient. However, the results of these showed little deviation in terms of pressure loss. The values of the total pressure drop presented from the steady state simulations are therefore an averaged value of the pressure in the last 1000 iterations after the fluctuations have stabilised around a relatively steady solution. A monitor plot of the pressure fluctuations at the inlet can be seen in Figure 6.3. The figure shows that the analysis with the finest mesh gave bigger amplitudes to the fluctuations. This is expected, as the fine mesh is able to capture the fluctuations better.

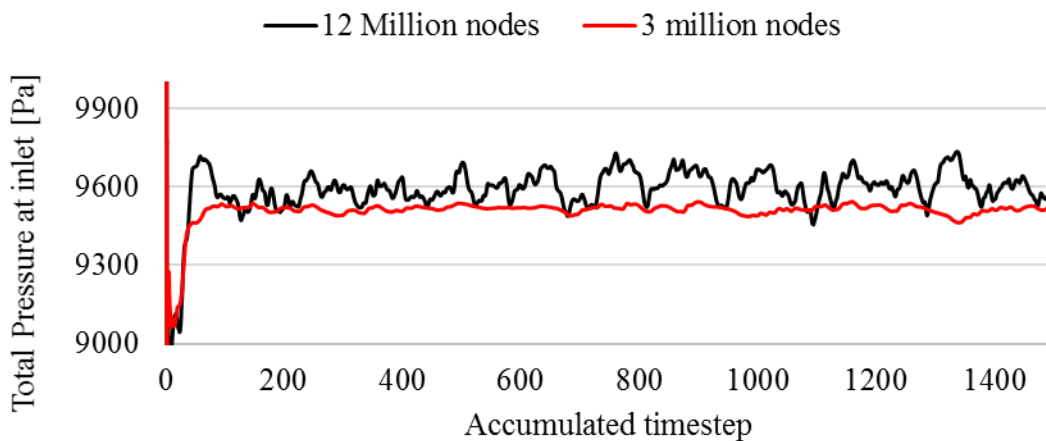


Figure 6.3 Monitor plot of the inlet pressure fluctuations of the finest mesh (12 million nodes) and the coarsest mesh 3 million nodes) in the $y^+ < 2$, steady state analyses.

Sensitivity of y^+

The y^+ sensitivity studies show that neither of the tested values of y^+ seemed to deviate significantly from the others. The pressure drop when increasing the first layer thickness to $y^+ = 300$ deviated only 1% from the case of $y^+ = 1$. Therefore, it is concluded that a y^+ of 100-300 will not lead to significant loss of accuracy in future simulations. This will ease the meshing process in the automated solver, as a fine tuning of the first layer thickness in the inflation layer will be unnecessary.

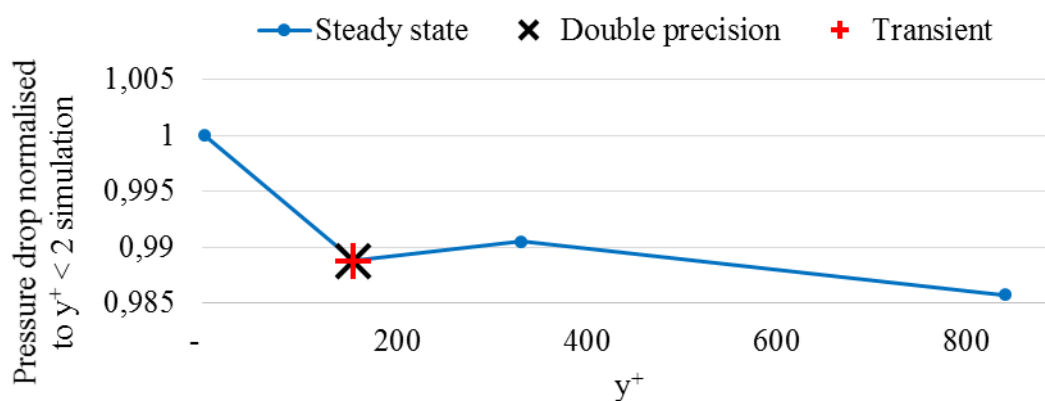


Figure 6.4 Results of the y^+ sensitivity studies performed at the 3 million nodes mesh.

Sensitivity of Mass Flow Rate

The results of the mass flow rate sensitivity tests displayed in Figure 6.5, shows that the simulations of the three mass flow rate cases converged at the same mesh resolution. Hand calculated values was obtained using the empirical formulas in theory chapter. The effects of the rock fall is difficult to calculate and was left out of the hand calculations. The simulations also showed that the pressure drop over the rock fall was very small compared to the pressure loss at the contraction into the pipe. It is worth noticing that the CFD results does not deviate significantly from the hand-calculated values. The second mesh, containing 3.6 million nodes is considered the mesh independent solution to the mass flow rate simulations. This mesh had a Hydraulic diameter/Body size ratio varying from 22.2 to 54.2 from the smallest to largest cross section.

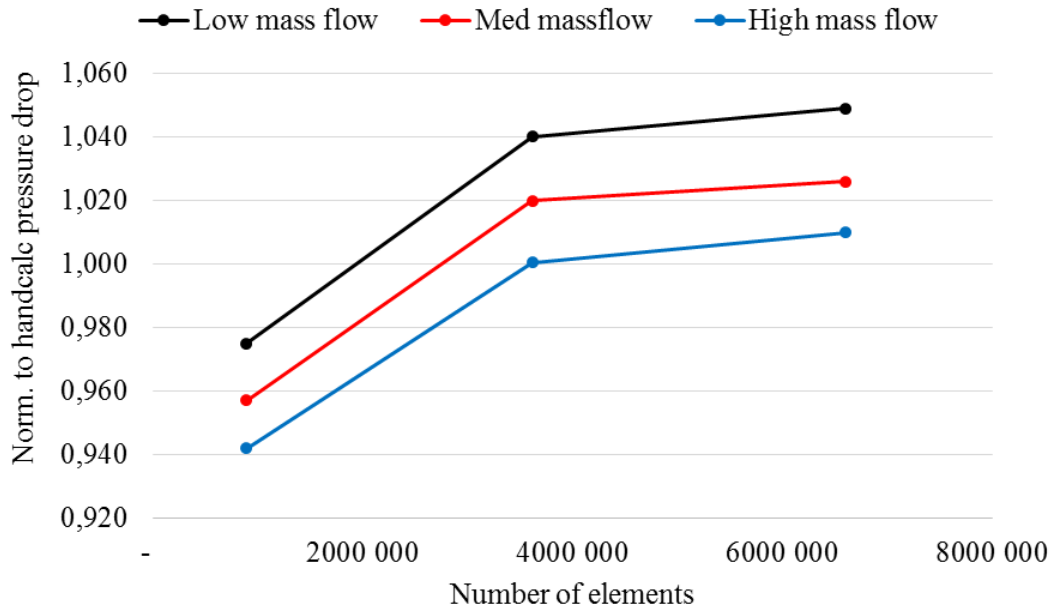


Figure 6.5 Mesh dependence test of Test Geometry 1 for different mass flow rates.

6.2 Test Geometry 2 - Nore Upper Sand Trap

The Statkraft hydropower station, *Nore*, is being upgraded and different options regarding sand traps are being considered. As part of the verification process of the automated CFD application, Statkraft provided drawings of the planned designs with details of the flow capacity. *Test Geometry 2* will therefore represent one of the proposed solutions to a sand trap in the system. The geometry was built in DesignModeler according to the construction drawings attached in Appendix C. A sketch of the geometry can be seen in Figure 6.6. The flow enters from the left and is decelerated by a gradual expansion. This will make the flow transported particles fall to rest and hopefully get settled in the sand trap. The sharp step will stop the particles from rolling into the section where the channel narrows and the velocities are increased.

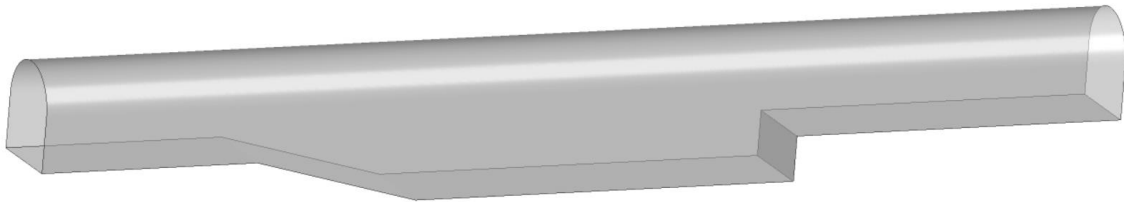


Figure 6.6 Test Geometry 2 – A sand trap in Tonstad Hydropower station. Flow direction is from the left to right.

In Test Geometry 1 it was decided that a relative high value of y^+ provided acceptable results. Therefore, the mesh dependency test of the upper sand trap was performed with first layer thickness of the mesh giving a y^+ value between 100 and 300. The geometry was built using DesignModeler and five meshes of increasing refinement was created in Ansys Meshing. The meshing was performed by specifying a body size for the whole domain and inflation layers were put at the wall boundaries. As opposed to the mesh in Test Geometry 1, which included regions of increased mesh density, the mesh in Test Geometry 2 has the same density throughout the domain. This is not ideal as complex parts of the model might get a little too few cells and other parts might get more cells than needed. However, in an automated solver, the level of automation is important, and in order to minimise the user intervention in the process, a general approach that provides acceptable results is preferred. The picture in Figure 6.7 shows the mesh around the corner of the step in the sand trap. This is a region with stagnation and creation of turbulence, which typically would require an increased mesh resolution. Based on the CFX mesh quality measures, all of the cells in the domain was within the “Acceptable” range.

For each of the meshes, simulations were run with three different mass flow rates specified on the inlet. Based on information from Statkraft, the maximum mass flow rate was set to 78 m³/s providing an average velocity of 1.29 m/s at the inlet section. The medium and low mass flow rates constitutes for 80% and 60% of the maximum mass flow rate respectively. The outlets was set as pressure outlets and the walls modelled as smooth walls with no slip conditions. The total pressure drop from the inlet to the outlet was monitored and used as measure for the convergence.

Table 6.2 Mesh details of Test Geometry 2.

Mesh	TG2-700K	TG2-1500K	TG2-3M	TG2-7M	TG2-14M
Number of nodes	736796	1588947	3234440	7267903	14000000
Body size [m]	0.35	0.25	0.18	0.13	0.10
First Layer thickness [m]	0.003	0.003	0.003	0.003	0.003
Y ⁺ (max)	207	225	224	230	238
Share of nodes within the range “Acceptable” mesh quality [%]	100	100	100	100	100
Hydraulic diameter/Body size ratio in sand trap	23.4	32.8	45.5	63.1	82.0
Hydraulic diameter/Body size ratio in tunnel	27.7	38.8	53.9	74.6	97.0

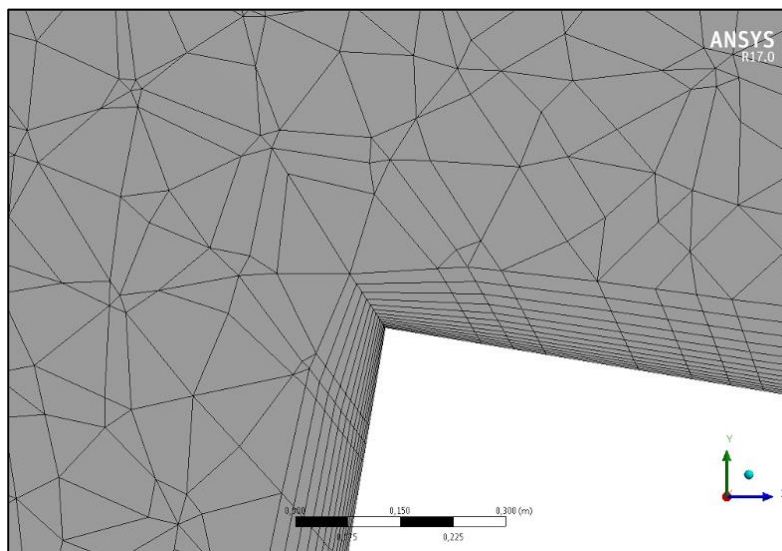


Figure 6.7 Capture of the mesh around the corner of the sand trap of Test Geometry 2.

Results and Discussion of Test Geometry 2

As can be seen in Figure 6.8 the calculated pressure drop stabilises as the mesh consists of 1.5 Million nodes and up. The CFD results seem to over predict the pressure drop over the geometry compared to the pressure drop calculated with empirical formulas. The hand calculated value is obtained using the empirical formulas from the Theory chapter. However, a small deviation from empirical formulas is expected as they are based on pipe flow and circular cross sections. Also in the analyses of Test Geometry 2 the pressure fluctuated in the steady state solution as the mesh got refined. The velocity contour plot in Figure 6.9 shows expected patterns with a stagnation zone upstream of the step and a recirculation zone downstream of the step. The mesh consisting of approximately 1.5 million nodes are consider to give a mesh independent solution. This gives a mesh independent hydraulic diameter/body size ration in the range of 32.8-38.8 for the different cross sectional areas of the geometry.

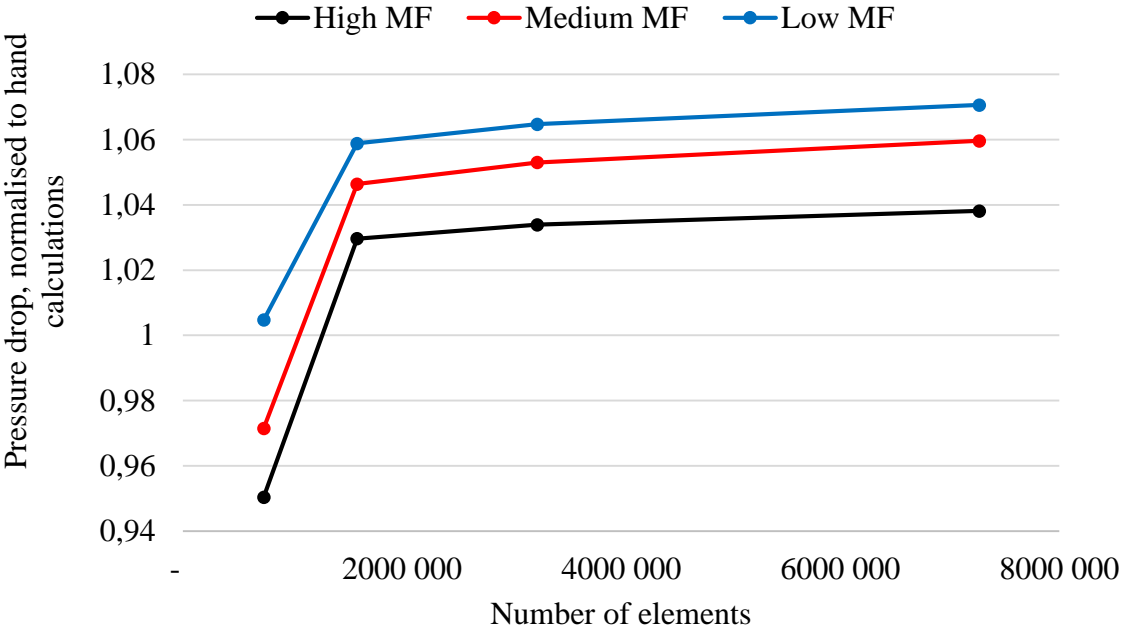


Figure 6.8 Normalised pressure drop in Nore upper sand trap. Pressure drop is normalised to pressure loss found by hand calculations.

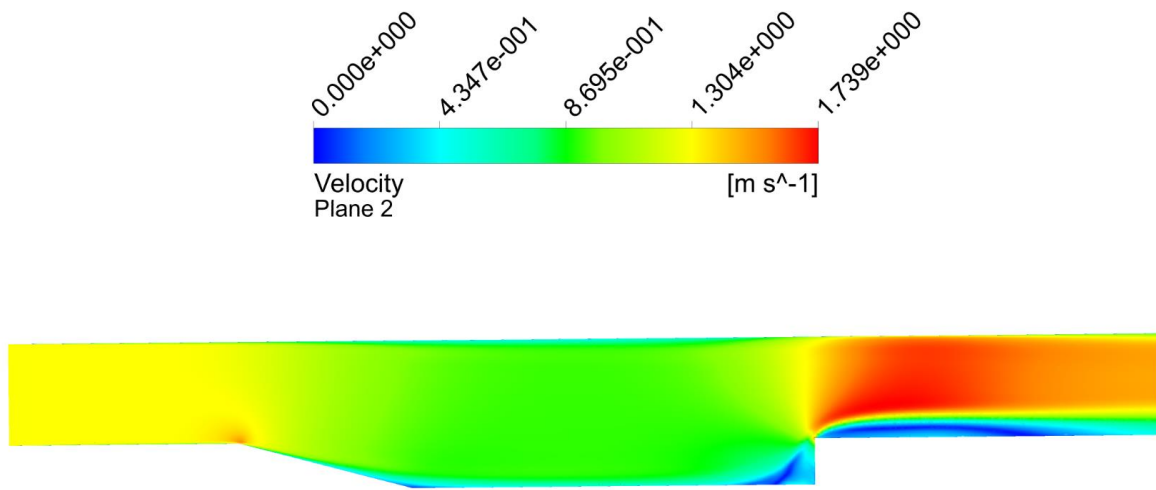


Figure 6.9 Velocity contour plot of the flow in Test Geometry 2.

6.3 Test Geometry 3 - Nore Lower Sand Trap

Another option to the sand trap described in the previous section is located further downstream in the Nore waterways and will be used as Test Geometry 3 of the mesh resolution study. The flow enters through the vertical, circular section that can be seen in the top right corner of Figure 6.10. Statkraft fears that this type of inlet to the sand trap will give the inflow a jet-like behaviour. Such jet will create turbulence that can erode and transport particles, such as sand and small stones. This is naturally unfortunate for sand traps, which should have the opposite function. Further, the flow is taken over a step to stop the particles transported along the bottom. The flow exits the domain through the three outlet channels, which is the start of the pressure shafts down to the turbines. The three outlets, seen from left to right on Figure 6.10, are named Outlet 1, 2 and 3 respectively. According to information from Statkraft, the outlets are specified with a given mass flow rate of $5.2 \text{ m}^3/\text{s}$ on Outlet 1 and $36.4 \text{ m}^3/\text{s}$ on Outlet 2 and 3. In order to get stability in the solver, the inlet is specified as a static pressure inlet.

The geometry was built according to the construction drawings provided by Statkraft, which can be seen in Appendix C. As in Test Geometry 2 it was initially attempted to do an automated meshing with specified equal body sizing and inflation layers throughout the domain. The CFD calculated pressure at Outlet 2 and 3 seemed to reach a converged solution at a global body size of 0.2 metres. In order to get convergence for Outlet 1 as well, a local refinement was introduced around the outlets. By keeping the global body size at 0.2 metres, the regions of increased refinement was meshed with decreasing body size. The quality of the mesh is considered “Acceptable” with regards to CFX quality measures described in the Theory section. The details of the meshes with local refinement can be seen in Table 6.3.

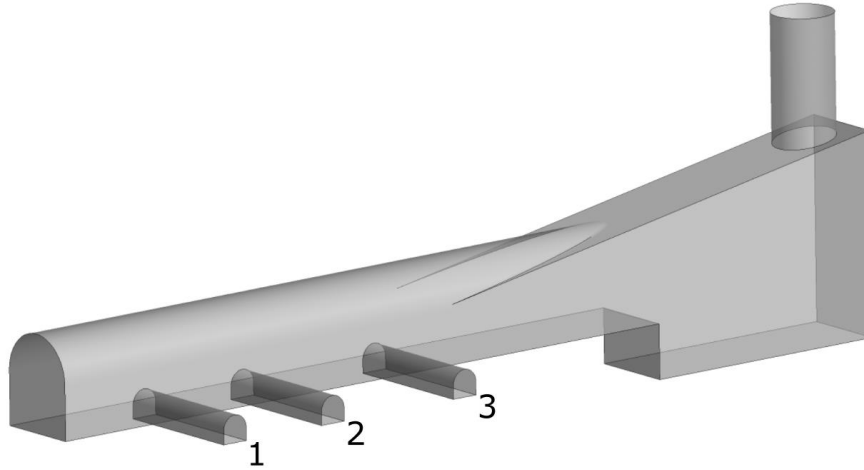


Figure 6.10 Test Geometry 3 - Nore lower sand trap.

Table 6.3 Mesh details of Test Geometry 3

Mesh	TG3- 2M	TG3- 4M	TG3- 8M	TG3- 13M	TG3- 40M
Number of nodes [Million nodes]	2.0	4.2	8.9	13.4	39.0
Main body size [m]	0.3	0.2	0.2	0.2	0.2
Refined region body size [m]	0.3	0.2	0.1	0.08	0.05
Nodes within the range “Acceptable” mesh quality [%]	100	100	100	100	100
Hydraulic diameter/Body size ratio in sand trap chamber	43.3	64.9	64.9	64.9	64.9
Hydraulic diameter/Body size ratio in transport tunnel (refined regions)	23.9	35.8	71.5	89.4	143

Results and Discussion of Test Geometry 3

As shown in Figure 6.12 the local mesh refinement in the outlet regions provided quite stable results for the Outlets 2 and 3. The pressure at Outlet 1 did not reach full convergence. This is most likely due to the pressure fluctuations, which also was experienced for the previous test geometries. The amplitude of the fluctuations seems to be of the same magnitude on all three outlets. However, due to the low mass flow rate at Outlet 1, the absolute value of the pressure is much smaller than for Outlet 2 and 3. This causes the percentage difference between the meshes to become bigger. Therefore, the mesh containing approximately 4 million nodes are accepted as mesh independent solution within reasonable limits. This provided an average Hydraulic diameter/Body size ratio of 64.9 in the big chamber underneath the outlet and 35.8 in the transport tunnel before the flow is taken to the outlets. As described earlier, the presented pressure values at the outlets are the average over the last 1000 iterations when the pressure monitor have reached a relatively stable solution. The complex geometry makes hand calculations using empirical formulas difficult and unreliable. Hence, the pressure values in Figure 6.12 are normalised to the pressure results given by the finest mesh.

The velocity contour plot in Figure 6.11 shows that the feared jet like behaviour of incoming water, when it enters the sand trap, seem to be present.

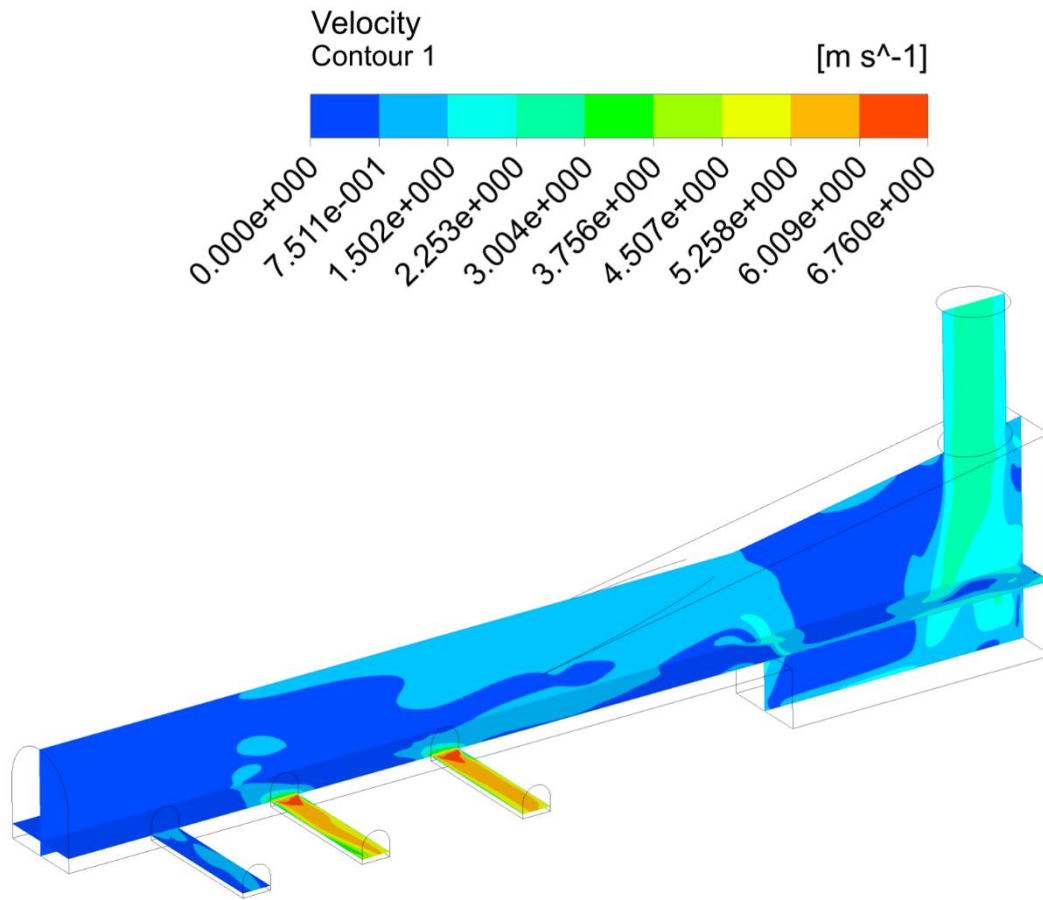


Figure 6.11 Velocity contour plot of the flow in Test Geometry 3 with High mass flow (78 m³/s).

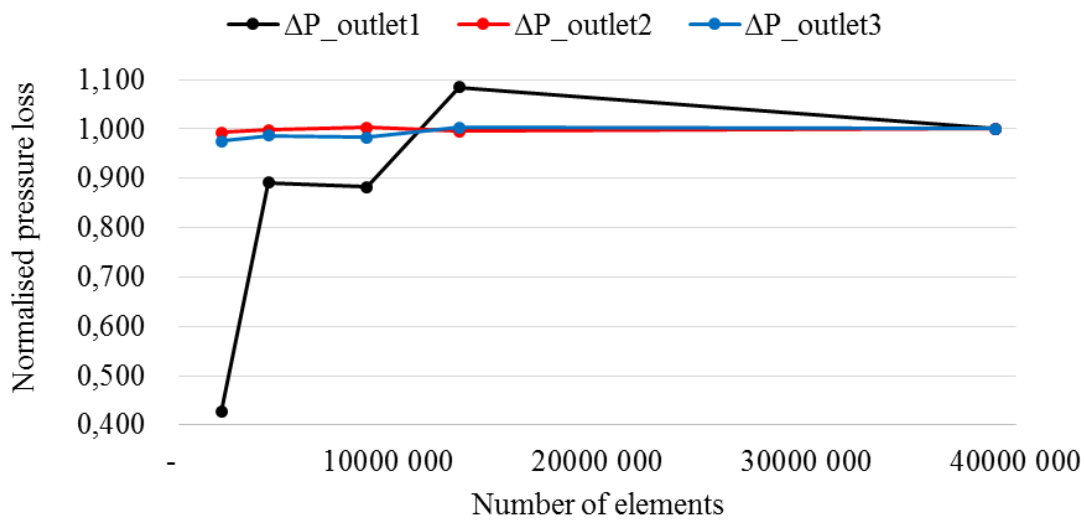


Figure 6.12 Pressure loss from inlet to the three different outlets at Nore lower sand trap with refinement of the mesh around the outlets. Normalised to the mesh containing the highest number of elements.

6.4 Conclusion of the Mesh Resolution Study

All of the tested geometries seemed to converge towards a mesh independent solution at an acceptable number of nodes in the mesh. The model was found not to be sensitive to mass flow rate and converged at approximately the same number of elements for different mass flow rates. The results of Test Geometry 1 and 3 show that local refinement in regions of complex flow situations, such as corners and contractions, is necessary. Even though Test Geometry 1 is of much smaller dimensions than the other geometries the required number of elements was approximately of the same magnitude. This is an indication that the required number of cells is related to cell count over a cross section, rather than the size of the elements. As mentioned in the introduction to this chapter, the ratio between the hydraulic diameter of a cross section and body size was investigated in all three analyses. Table 6.4 displays the ratio between hydraulic diameter of cross sections in the domain and the body size applied in the mesh independent mesh. As the geometries tested in this chapter have a large variation in cross sectional measures, the ratio varies from 22.2 to 64.9. A value in this range might therefore be an appropriate starting point for the mesh resolution of every cross section in the geometry. In geometries with big variation in the cross sectional area, it might be beneficial to split the geometry and use local body sizing. This will prevent the use of an unnecessary fine mesh in large regions without significant complexity and thus reduce computational cost.

Additionally, the user of the automated solver will be able to build models of a large range of complexity. Hence, the required mesh resolution will vary from case to case. One opportunity could be to always run an additional analysis with an increased density of the mesh. Deviations in the results of the two simulations would indicate that further investigations is required in order to get a reliable solution.

Table 6.4 Ratio of hydraulic diameter of cross section versus required body size of mesh independent solution for Test Geometry 1, 2 and 3.

Test Geometry	TG1	TG2	TG3
D_H / Body size , small cross section	22.2	32.8	35.7
D_H / Body size , big cross section	54.5	38.8	64.9

7 CFD Analyses of Rough Surfaces

The previous chapter showed that the automatic CFD application would be able to give a representative picture of the flow in typical hydropower geometries, on a conceptual level. So far, the analyses have regarded tunnels modelled without roughness at the walls. The waterways in hydropower systems are often blasted out using explosives, leaving a very rough and uneven surface on the walls. The roughness contributes to friction losses, but it also distorts the laminar near wall boundary layer and causes turbulent regions along the wall. In order to get a correct picture of the flow in the tunnels, this roughness will have to be accounted for in the CFD analyses.

As described in Section 4.5 in the CFD Theory chapter, there are several ways to account for the roughness in CFD analyses. One opportunity, and the most straight forward, is to apply the roughness wall model of CFX, where the near wall velocity profile is shifted towards the wall. As this applies to the wall laws of the first cell in the mesh, it is only valid when the roughness height is smaller than the first cell in the mesh [2]. In hydropower tunnels, the RMS roughness height is typically of magnitude 0.35 metres [6], which is much bigger than what the cell size on the walls have to be. Hence, the rough wall boundary conditions can not be applied directly for waterways analyses of blasted tunnels. Initial studies performed with the rough wall models confirmed this invalidity.

Another approach to model the roughness is to add porosity to the cells of which contain the roughness elements. This approach have shown good results compared to field measurements when analysing stretches of rivers [17]. However, this approach is not investigated in this master's work, as it will not be implemented in this stage of the automated CFD application development. On the other hand, it might be implemented in the future.

The third approach involves simulating the rough surfaces by letting a fine mesh cover the boundary of the roughness elements. Here it is possible to apply laser scans of the actual tunnel or generate a geometry with physical roughness elements. Alternatively, it is possible to create a smooth geometry and mesh it accordingly, but later pull in the nodes at the wall so that the mesh is formed like a rough domain. Laser scans of real tunnels would provide a precise representation of the rough geometry and reduce the uncertainties regarding geometry

deviations from construction drawings. However, as the automated solver is supposed to be used on a conceptual level, this accuracy is not required. Hence, only the approach of geometry manipulating and the mesh deformation approach will be investigated and is presented in Section 7.1 and 7.2. A summary and conclusion of the roughness studies will be given at the end of this chapter, in Section 7.3.

7.1 MATLAB Generated Rough Geometry

This section involves the studies of a 100 metres stretch of a straight tunnel with a standard tunnel cross section as described in the Theory section. The aim is to investigate how well a rough geometry created using MATLAB is representing typical roughness of blasted hydropower waterways. Additionally, we want to see how well the SST turbulence model is able to capture the turbulent effects caused by the roughness.

The geometry surfaces was built in MATLAB by creating a surface mesh consisting of points created by a random function. In order to get a representative blasted tunnel roughness the IBA method [19] described in the Theory section was applied. The root mean square of the roughness elements was 0.33 meters with a maximum amplitude of 0.6 meters. In order to avoid sharp geometry changes, such as thin spikes and cracks, the distance between the roughness elements in the longitudinal and circumferential direction was set to 0.5 meter. The IBA method requires measurements every 0.25-0.5 meter [19], thus the distance between the roughness elements in the generated geometry is within this range. A RMS roughness of 0.33 meter is quite similar to the roughness found by Bråtveit in her analyses of Tonstad Hydropower station [6]. Inserted in the Equation 3.5 and 3.8 the RMS roughness provide a Darcy friction factor of 0.056 and a Manning number of 31.4 which is quite close to the typical Manning numbers of blasted hydropower tunnels [11]. The MATLAB code for generating the geometry can be found in Appendix A.

The MATLAB generated surfaces was later imported to SpaceClaim, which is an Ansys owned CAD software. In SpaceClaim, the function *Skin Surface* was applied on the MATLAB surface to create a domain volume. SpaceClaim was preferred over DesignModeler, as it allows import of such surface files (.stl).

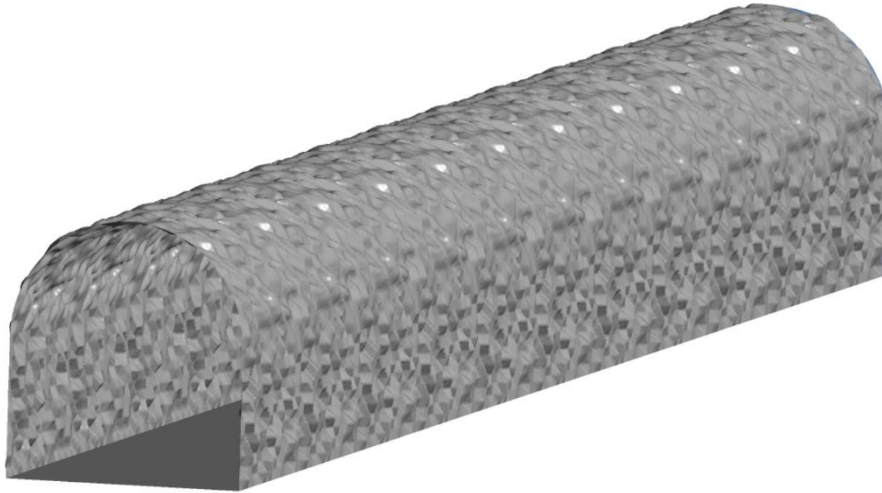


Figure 7.1 Blasted tunnel geometry replica created in MATLAB and SpaceClaim.

Meshing MATLAB Rough Geometry

The meshing of a rough geometry involves a very fine mesh along the walls in order to capture the roughness elements. Using a too coarse mesh will wash out the roughness and not be able to resolve the boundary layer of the elements. The meshing was performed using Ansys Meshing with inflation layers at the wall and a body sizing to control the element size in the free flow. Near the wall, the element size is decided by default tolerances and expansion ratios in the ANSYS Meshing. To simplify the meshing process, only 10 meters of the model was built with the aim of duplicating it in the lengthwise direction at a later stage. To be able to do this, the mesh at each side of the subdomain will have to be equal in order to get a smooth transition between the meshes. This was accomplished using the Ansys Meshing function *Match Control*. As the floor in hydropower tunnels are used as transport roads under the construction of the tunnels, they do not have the same rough surface as the walls. Hence, the floor is modelled as a regular wall with no slip conditions. In order to get a decent mesh in this region a face sizing was applied to the floor. The mesh details can be seen in Table 7.1. The quality of the mesh is good and within the Ansys CFX range of “Acceptable” quality, except for the maximum expansion factor measure. However, this only apply for a small fraction of the nodes, as 100 percent of the nodes are within the acceptable range. The cross sectional view of the mesh in Figure 7.2 shows a very fine mesh throughout the cross section with an extra refinement on the walls. The inflation layers are very thin and is not visible on the figure, therefore a closer view is given in Figure 7.3.

Table 7.1 Mesh details of the MATLAB generated rough geometry analyses.

Properties	Mesh
Body size [m]	0.3
Face size floor [m]	0.1
First layer thickness [m]	8e-6
Number of nodes	46 000 000
Y ⁺	1.09
Max Aspect ratio	26764
“Acceptable” Aspect ratio [%]	100
Max Expansion factor	39 (!)
“Acceptable” Expansion factor [%]	100 (<1 % unacceptable)
Max Orthogonal angle	20.8
“Acceptable” Orthogonal angle [%]	100

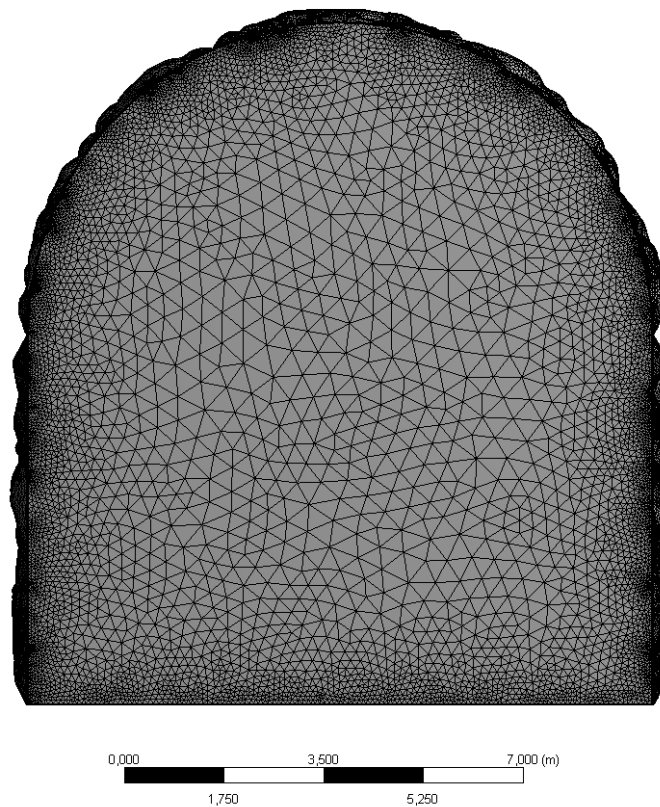


Figure 7.2 Cross sectional view of the mesh in the MATLAB generated geometry.

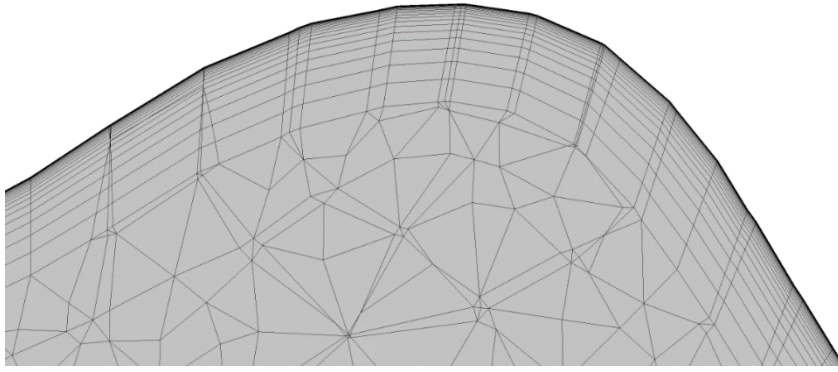


Figure 7.3 Zoomed in on the mesh around a roughness element. Due to the $y^+=1$, the inflation layers closest to the wall are too thin to be visible on the picture.

Setup of the MATLAB Roughness Simulation

In order to see how well the CFX solver can provide a correct picture of the flow in the rough tunnels, three types of analyses was performed. The first analysis was the Steady State analysis using the SST model for turbulence. In order to check for time dependent effects, a transient simulation was run of the same case. A SAS analysis was also performed as a control to see how well the SST model captured the level of turbulence created by the rough walls. As mentioned in the Theory chapter, the SAS analysis utilises Large Eddy Simulation in the free flow, and SST with wall functions near the wall. This is a computational expensive analysis, that requires a very fine mesh and $y^+ = 1$. The y^+ requirement of the SAS simulations leads to a very thin first layer thickness of the inflation layers. As the expansion ratio of adjacent cells should be kept within reasonable values, the number of cells is very high in this analysis. As it also is a transient simulation that require relatively small time steps, the simulations requires several hours of computing time on a relatively powerful computer. Hence, the SAS analyses and also the transient simulations with SST turbulence models are not applicable in the automated solver due to high computational cost. However, the results of the analyses will provide good basis for comparison to the steady state analyses.

The inlet was specified with a velocity of 1 m/s and the outlet as pressure outlet with a static average pressure of zero Pascal. The walls were modelled with no slip conditions. First, the steady state analysis was simulated until the pressure loss over the geometry had reached a steady state solution. The transient simulations was initiated from the steady state solution in

order to save time as the flow is already developed. The transient simulations was run for a simulation time of 40 seconds with a time step of 0.01 seconds. The low time step is required to maintain a low courant number that will make the results more accurate.

Results and Discussion of the MATLAB Geometry Analyses

The pressure drop is measured by looking at the difference in the mass flow average pressure at the cross section at $z=80$ m and the outlet. Only the last 20 meters of the tunnel is used for pressure loss measurements in order to measure the developed region of the flow. The hand calculated values is obtained using Equation 3.6 from the theory chapter with a Manning number of 31.5. The results in Table 7.2 show that the SAS simulations provided the most correct pressure drop compared to hand calculations. This is expected as the model captures the turbulent effects on a higher level than the SST model. The SAS deviated from the hand calculated values with only 12%. With the uncertainties regarding the Colebrook equation in mind (Equation 3.5), it seems that the MATLAB generated geometry is representative for blasted hydropower waterways. The pressure drop in the SAS simulations yields a Manning number of 35.7, which also is within the range of typical Manning numbers in hydropower applications [11]. Another source of deviations from the Colebrook equation is the fact that the floor of the tunnels are not simulated with roughness elements.

The idea of the applied roughness is not to represent a specific tunnel geometry, but to create a general tunnel roughness to get representative flow conditions. The actual blasted geometry will deviate from the plans anyway due to unstable rock, miscalculated amount of explosives and similar. The velocity contour plots in Figure 7.4 shows that the SAS analysis get some regions of slightly higher velocities than the SST analyses. This might be because in the SST analysis, the velocity is averaged in time, hence the velocity gradients are smeared out. This could be critical when it comes to analysing sediment transport, as increased velocity would make the flow able to transport particles of larger diameter. On the other hand, the turbulent kinetic energy plots in Figure 7.5 and Figure 7.6 show that the SST simulations provide higher levels of turbulence than the SAS, which indicates that there will be rapid changes in the velocity. Overall, it seems that steady state simulations provide reasonable representations of the flow in rough surfaced tunnels and offers a fair compromise between accuracy and computational cost.

Table 7.2 Results of the analyses on the rough tunnel geometry created in MATLAB.

Case	Number of nodes	Y+	Pressure drop normalised to hand calculations
SST Steady State	46 000 000	1	0.77
SST Transient	46 000 000	1	0.74
SAS Transient	46 000 000	1	0.88

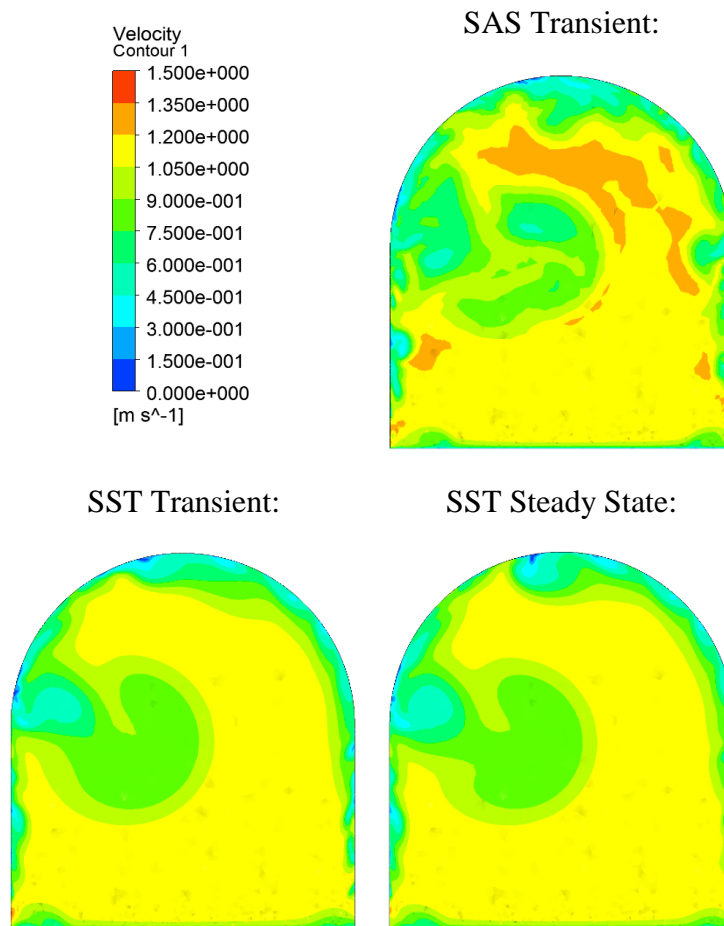


Figure 7.4 Cross section velocity contour plot of the MATLAB geometry. Cross sections are located 70 m down stream of the inlets.

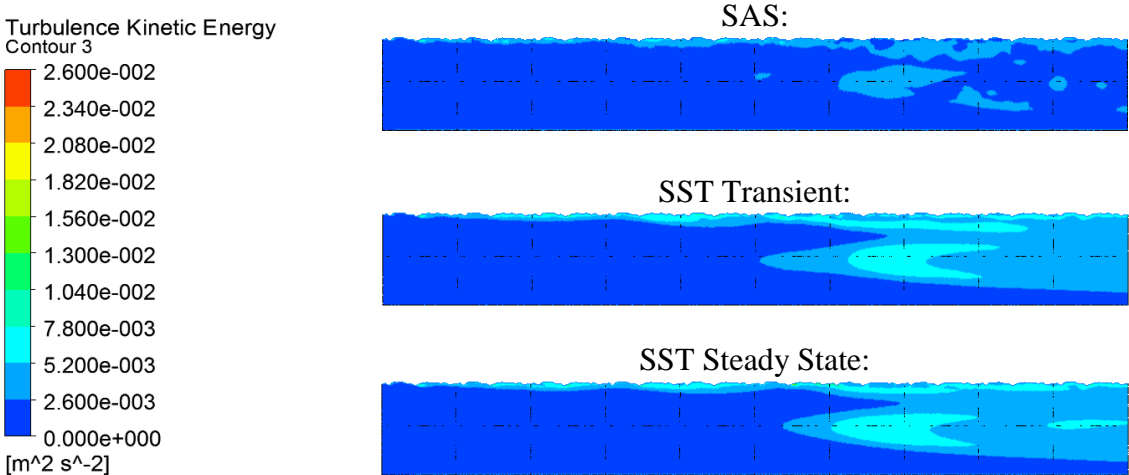


Figure 7.5 Longitudinal contour plot of turbulence kinetic energy through the centre of the tunnel. Flow direction from left to right.

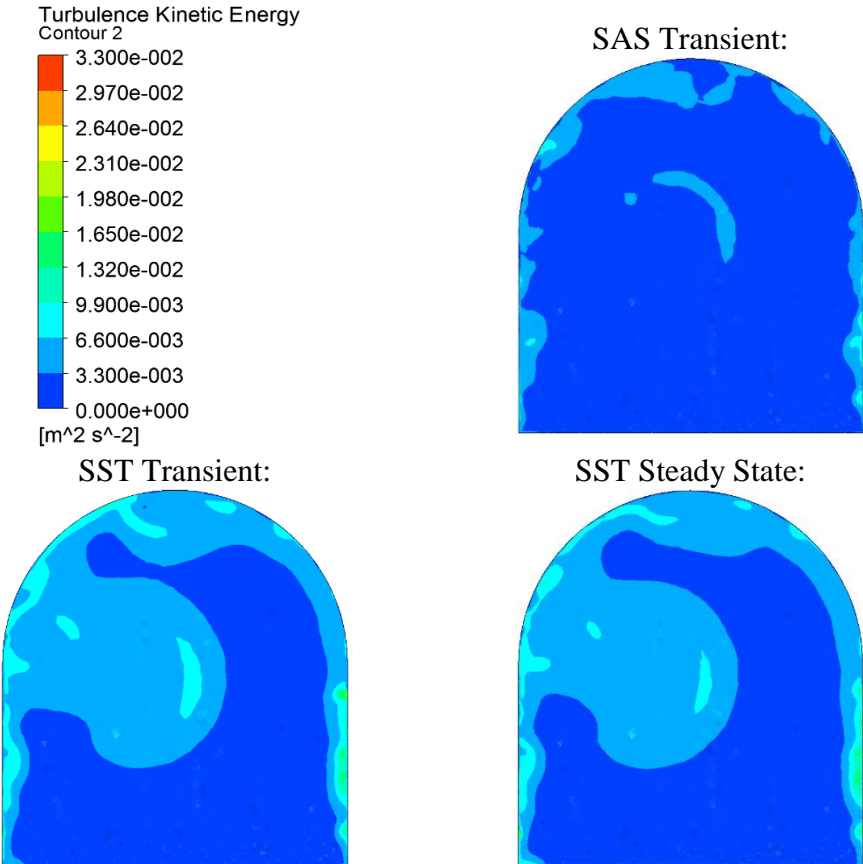


Figure 7.6 Cross section turbulent kinetic energy contour plot of the velocity 70 meters downstream of the inlet in the MATLAB generated geometry analyses.

7.2 Mesh Deformation to Simulate Roughness

The mesh deformation approach to simulating the roughness involves creating a mesh around a smooth geometry, and later create the roughness elements directly in the mesh by pulling the nodes. Because the mesh will constitute for the roughness, the elements can be quite coarse without cutting of the corners of the roughness. The nodes can be pulled for instance according to a sine function, leaving a sine wave surface boundary. By using the *CFX Expression Language (CEL)*, the amplitude and frequency of the sine wave can be specified. This also makes it possible to integrate the rough walls in the automated CFD application.

Geometry, Meshing and Setup

The measures of the geometry investigated, is the same as for the MATLAB generated rough geometry investigated in the previous sections. A smooth geometry was created in DesignModeler and meshed according to the mesh requirements found in the Mesh Resolution study in Chapter 6. In CFX-Pre a node displacement was defined by adding a *Specified Location* to the wall and ceiling boundaries. The specified location of the nodes was given by expressions defined in the *CFX Expression Language (CEL)*. The nodes was pulled normal to the surface boundary and in a sine wave oscillating pattern in the longitudinal direction. The amplitude, a , of the sine function was defined $a = 0.33$ metre, equal to the desired RMS roughness height. The significance of the wavelength, λ , was investigated by simulating both $\lambda = 5.0$ metres and $\lambda = 3.3$ metres. It was also attempted to include an even shorter wavelength, but this resulted in errors due to mesh being too distorted to maintain acceptable quality of the mesh. By giving the remaining surfaces, *Unspecified Mesh Motion*, a smooth transition between the rough and non-rough surfaces is ensured. In order to prevent distortion of the mesh and creation of cells of negative volume, the *Mesh Stiffness* is set to its maximum value of $1e15 \frac{m^2}{s}$. It is also important to set the mesh displacement only to occur on the first iteration. Pictures of the domain and the mesh is seen in Figure 7.7 and Figure 7.8.

The simulations was steady state analyses with SST model for turbulence. The inlet boundary was defined with an average velocity of 1 m/s and the outlet with a zero Pascal static average pressure boundary condition. The pressure drop was monitored from inlet to outlet and used as measure for the convergence.

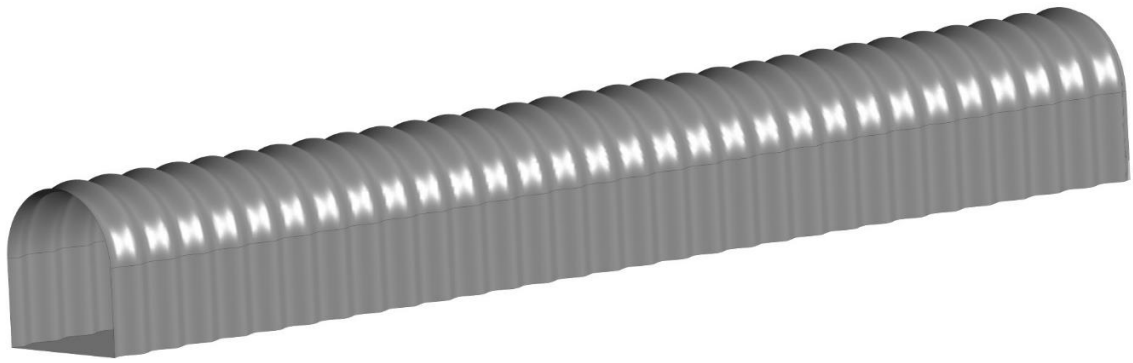


Figure 7.7 Domain representation of the simulation with mesh deformation.

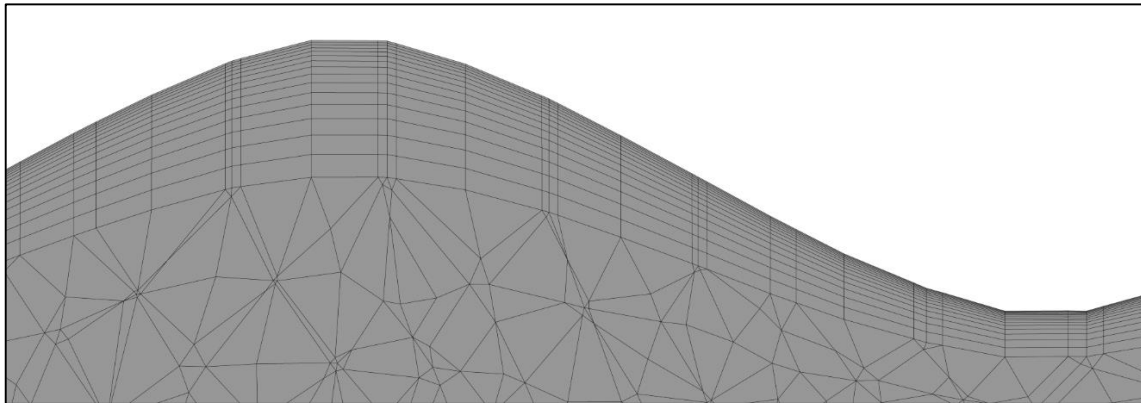


Figure 7.8 Capture of the mesh around the roughness elements in the domain created by mesh deformation.

Results and Discussion

The velocity contour plots of the two simulations in Figure 7.9 shows that the sine wave roughness is able to distort the near wall boundary. The flow seems to be close to a developed state in the last region of the tunnel. Hence, the pressure drop was measured over the last 10 metres stretch. As it is also shown on the contour plots, the pressure drop results presented in Table 7.3 show that the wavelength is of great significance when it comes to giving a representative picture of the pressure loss due to friction. The hand calculated pressure loss for a geometry of with RMS roughness 0.33 metres, calculated with Equation 3.5, 3.6 and 3.8, lies in between the CFD results of the two wavelength simulations. The flow in the tunnel with the

shortest wavelength appears to be more centred on the middle of the tunnel and higher velocities occur in this region.

Even though the numerical results did not match the hand calculated values of pressure drop, the concept of roughness generation by deformation of the mesh is promising. The procedure is quite simple to include for various geometries, and hence suitable for the automatic CFD application. However, the results of this investigation show that the approach require more investigations in order to become robust enough to give acceptable results. Tuning of a representative amplitude and wavelength of the sine waves is required. It would also be necessary to test for various sizes of cross sections in order to investigate the effect of the relative roughness.

Table 7.3 Pressure drop in analysis of rough surfaces by mesh deformation.

Wavelength	CFD Pressure drop. Normalised to hand calculations
$\lambda=3.33$ metres	1.43
$\lambda=5.0$ metres	0.53

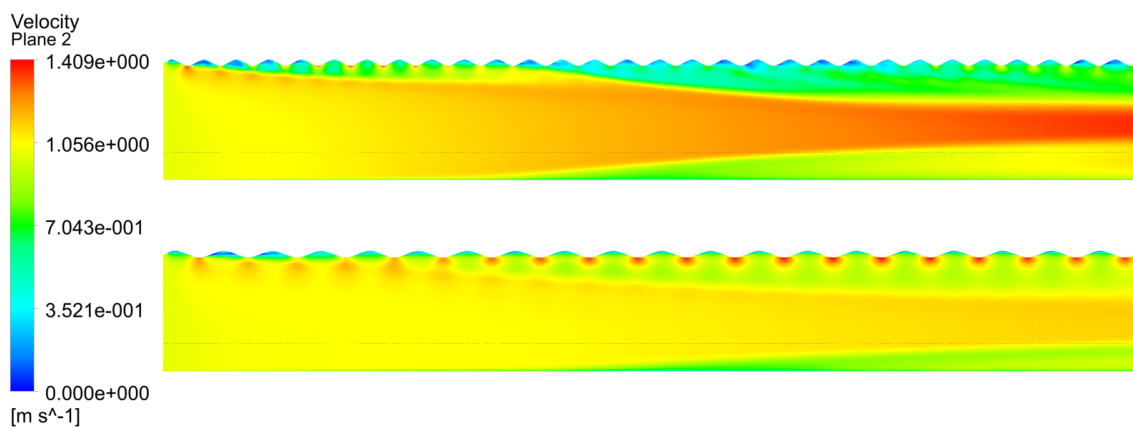


Figure 7.9 Velocity contour of the SST steady state simulations of the rough surfaced tunnel with mesh deformation. The top image is the $\lambda=3.33$ m and the bottom is $\lambda=5.0$ m.

7.3 Conclusion of the Roughness Studies

In this chapter, various methods of implementing the roughness effects of blasted tunnel walls in the automated CFD application have been investigated. The CFX Rough Wall model alternative was rejected at an early stage, as the model is invalid for roughness height of magnitude bigger than the height of the first cell in the mesh. Therefore, it is concluded that the roughness elements must be simulated, rather than modelled.

The SAS simulations of the rough geometry generated in MATLAB show good results compared to theory, with only 12% under estimation of the pressure loss due to friction. The SST simulations show similar trends in flow pattern and turbulence, but under predicts the pressure drop due to friction by roughly 25%, compared to hand calculations. However, due to the uncertainties related to the empirical formulas for friction loss and the lack of accuracy in the blasting of the tunnels, the MATLAB generated rough geometry is considered to be a good representation of blasted hydropower waterways.

The SAS analyses require large amounts of computational resources, and hence not appropriate for the automatic CFD application. SST offers shorter simulation time, at the price of a decrease in accuracy. However, in order to simulate the roughness elements, a very fine mesh is required in order to resolve the boundary layer and the geometrical shape of the elements. This also applies for the steady state SST analyses, and they may also become too heavy for the automated CFD application.

The simulations of rough surfaced tunnels with the mesh deformation approach show promising results with regards to computational time and relatively simple implementation. However, the results showed a significant dependence on the wavelength of the sine wave of which the surfaces was fitted to. This implies that additional investigations is required in order to achieve a representative roughness with regards to pressure drop. Several analyses with different geometries should be run in order to quantify the uncertainties regarding the roughness implementation.

8 Sediment Transport

Sediment transport is an important field of study in hydropower systems. In certain flow conditions, particles of various sizes can be transported in rivers, streams and waterways. Some hydropower plants have issues with erosion wear on the turbine blades due to sand transport over the turbine. Others have issues with stones of larger sizes causing instant damage when they are transported through the turbines [5]. This chapter will investigate the ability of the CFX solver to simulate particle transport in hydropower systems in order to avoid such damages. The first part of the chapter will include particle tracking analyses of Test Geometry 3. The method and procedure of the analyses will be described together with a presentation of the results and a short discussion. In the next part of the chapter, analyses of sediment transport in Test Geometry 2 is performed, in order to see how changes in geometry affects the results. Comparisons to empirical formulas for sediment transport are also performed for the Test Geometry 2 analyses. At the end of the chapter, there will be given a short conclusion to discuss the ability of the automated CFD application to simulate sediment transport.

8.1 Test Geometry 3 – Sediment Transport Study

Procedure

As described in Section 4.6, there are several ways of simulating particle transport in CFD. For the automatic CFD application, the *Eulerian-Lagrangian* approach is assumed the most appropriate model, because of its relatively simple implementation, compared to for instance the Eulerian multiphase methods. In CFX the Eulerian-Lagrangian approach is called *Lagrangian Particle Tracking*. The Algebraic slip method was also considered, but this is not investigated further in this project. This is because of the issues with the particle wall interaction, as described in Chapter 4.

Hence, Lagrangian Particle Tracking is applied on the mesh independent steady state solution of Test Geometry 3. The initial analyses showed that a high share of the particles experienced the fate of integration error. This was resolved by running the simulations with *double precision*. As described in the theory section, this increases the accuracy in the particle tracking calculations and reduces the risk of round off errors.

First, the number of particles released on the surface was analysed. Being a statistical analysis the aim is to find how many particles that needs to be released in order to get a representative solution regarding the particle diagnostics. Therefore, simulations were run for 100, 1 000 and 10 000 particles uniformly distributed on the inlet. All of the simulations included particles with diameters of 0.5, 1.0 and 2.0 millimetres.

If a particle falls to rest inside the sand trap, or get stuck in a turbulent vortex, it will be tracked until the limits of either time, distance or integration steps are reached. The magnitude of these limits is also investigated. If a particle follows the centre of the waterway, from the inlet to the outlet on Test Geometry 3, the distance travelled will be approximately 150 meters. With the average velocity at the different cross sections taken into account, this will provide a travel time of 200 seconds. By multiplying the typical travel distance and time with a time/distance factor the limits of time and distance are found. To check for the effect of tracking time and distance, factors of 10, 100 and 1000 was analysed. All the simulations was run on the same computer with the same number of cores assigned to the simulations. This was done in order to compare the simulation time of the different simulation setups.

The restitution coefficient was set to 1.0 for both parallel and normal interaction with the wall, as this is the most conservative option with regards to particle transport through the domain. This means that when a particle bounces into a wall, the kinetic energy is conserved. The drag force option was the Schiller Neumann. Virtual added mass, turbulence dispersion force and pressure gradient force was included as non-drag factors. Gravity was specified in the negative y direction.

Results and Discussion

The results in Table 8.1 show that a fraction of all of the tested particle diameters made it all the way to the outlet. No clear trend is seen by increasing number of particles, hence 100 released particles would be acceptable for this case. However, 1000 particles is chosen as recommended number of released particles, as it provides increased robustness and also had an acceptable computational time. The magnitude of the time/distance factor does not seem to influence the results significantly, hence a factor of 10 is considered acceptable in the automated CFD application. Particle tracks of the tested particle diameters are presented in Figure 8.1. In the pictures, the number of particles released is 1000 and the time distance factor is set to 10.

Table 8.1 Particle statistics of the analyses of Test Geometry 3.

Number of particles tracked:	100	1 000	10 000	100	100	1000
Time/distance factor	10	10	10	100	1000	100
Particle diameter 0.5 mm	52%	57.2 %	55.83%	52%	54%	58.4 %
Particle diameter 1.0 mm	27%	27.9 %	27.88%	27%	27%	27.9 %
Particle diameter 2.0 mm	4%	3.4 %	3.67%	4%	4%	3.5 %
Computational time [minutes]	3	20	170	18	46	150

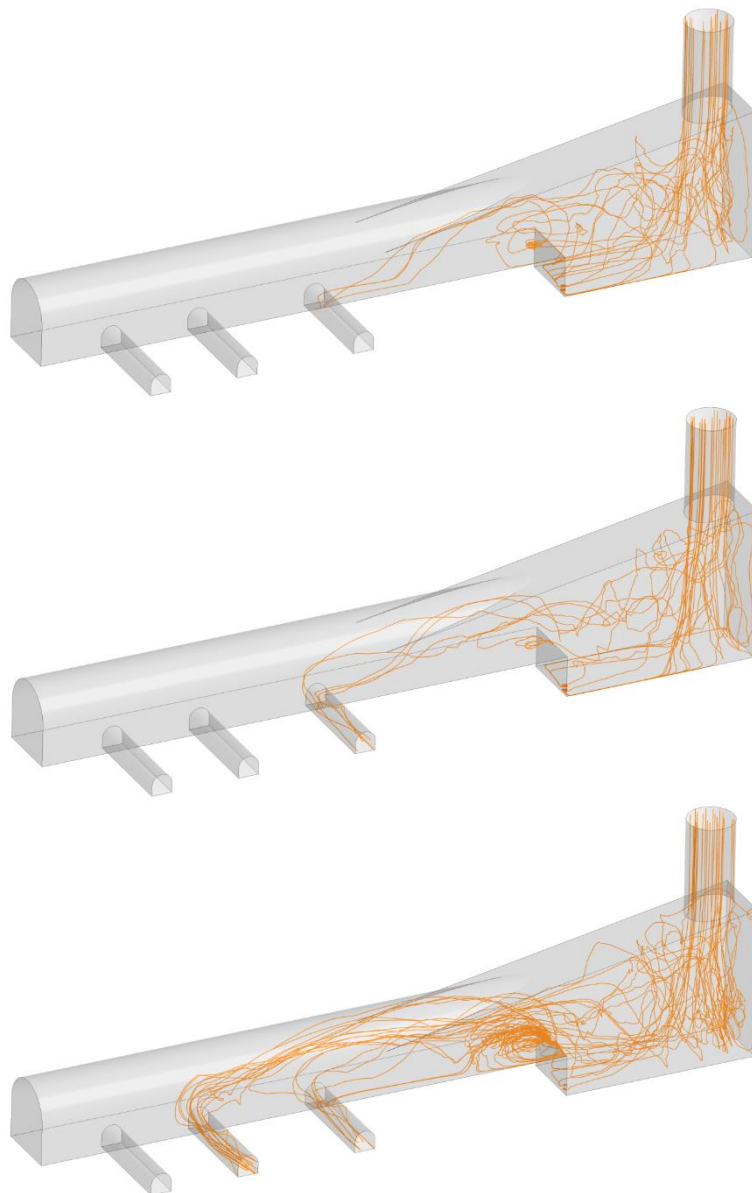


Figure 8.1 Particle trajectories of the particles released on Test Geometry 3. The top picture shows particle of diameter 2.0 mm, the middle 1.0 mm and the lower picture shows 0.5 mm particles.

8.2 Test Geometry 2 – Sediment Transport Study

Procedure

Sediment transport analyses was also performed on Test Geometry 2 in order to compare the results with hand calculations of the sediment transport using empirical formulas. Particles in the range of 0.1-10 millimetres was released on the mesh independent steady state solution of Test Geometry 2 analyses in Section 6.2. Due to the findings regarding number of particles to be tracked, these analyses was only performed with 1000 particles released on the inlet boundary and a time/distance factor of 10.

Results and Discussion

As seen in Table 8.2, only particles with diameters smaller than 1 millimetre was transported all the way to the outlet. The mass flow was specified as $78 \text{ m}^3/\text{s}$ and the cross sectional area of the expanded part of the sand trap is 91 m^2 . This provides a mean velocity in the sand trap of 0.86 m/s . According to Hjølström's diagram, described in Figure 3.6 in the Theory chapter, this would make the flow able to erode particles of diameter up to 4 millimetre.

By applying the wall shear stress found on the bottom by the CFD analyses, the particle diameter of which the flow is able to transport, can be calculated from Equation 3.10 in the theory section. As pictured in the contour plot in Figure 8.2, the maximum shear stress on the bottom in the middle of the sand trap was found to be 1.3 Pascal. According to Equation 3.10, this should initiate the movement of particles smaller than 1.3 millimetres. This is also similar to the results using the formula in Equation 3.14, that with a C_p coefficient in the range of 115-140, provides a critical particle diameter of 1.5-1.8 millimetres.

A possible reason for the deviation between the CFD results to hand calculated values can be seen in the particle trajectory plots in Figure 8.3. If a particle hit the bottom it is never eroded back into suspension. Even when the smallest particles hit the bottom, they are just dragged along the bottom instead of being re-suspended by the turbulent forces. Also the particles falling to the bottom in the inlet region of the domain is not being re-suspended, despite the high shear stress seen to the left in the contour plot. Hence, the Lagrangian Particle Tracking fails to model the erosion and is thereby not giving a correct picture of the transport of particles along the bottom. This also confirms the findings by Vasquez [23].

Table 8.2 Particle statistics of the analyses on Test Geometry 2. Showing share of particles being transported all the way to the outlet.

Number of particles tracked:	1000
Particle diameter 0.1 mm	96.8 %
Particle diameter 0.4 mm	48.8 %
Particle diameter 0.6 mm	20.6 %
Particle diameter 0.7 mm	8.2 %
Particle diameter 0.8 mm	2.2 %
Particle diameter 1 mm	0
Particle diameter 5 mm	0
Particle diameter 10 mm	0
Computational time [minutes]	11

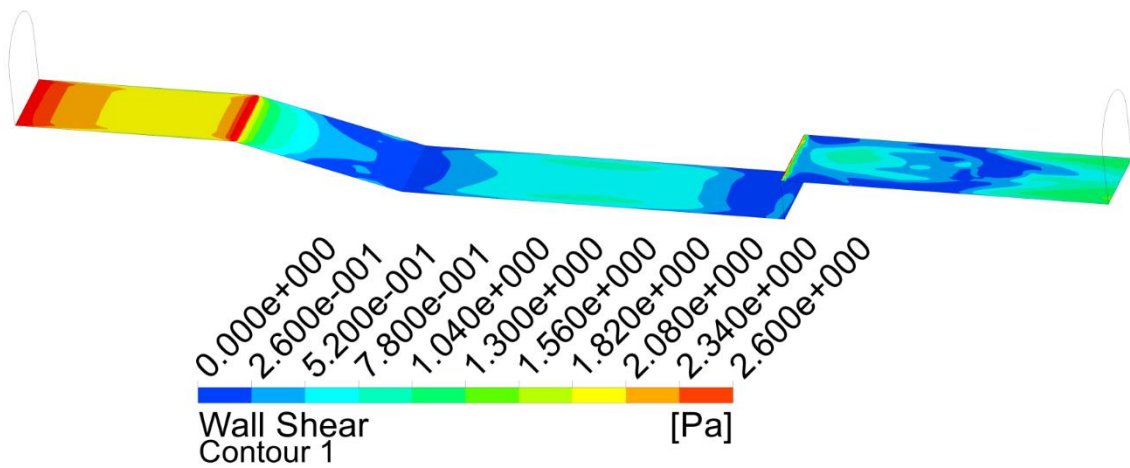
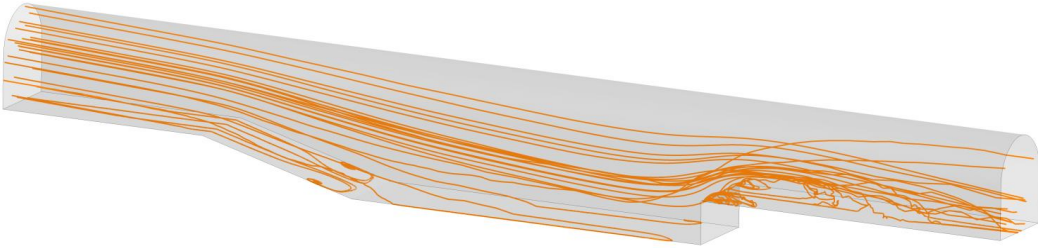
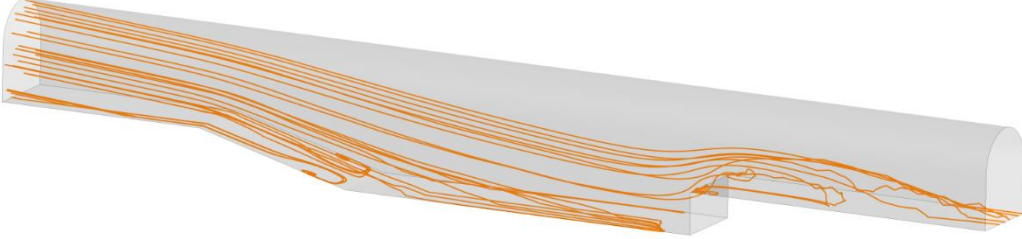


Figure 8.2 Contour plot of the shear stress on the bottom of Test Geometry 2. Flow direction is from left to right.

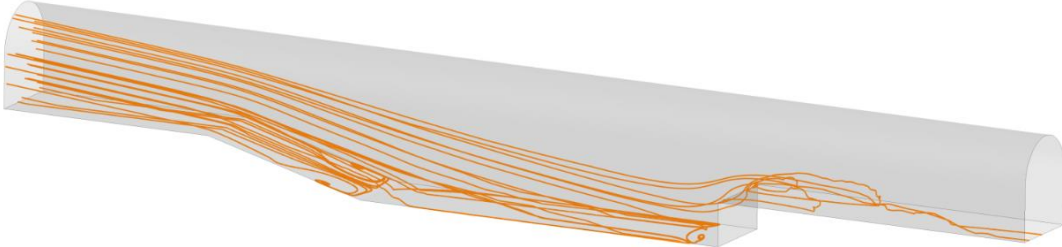
0.4 mm particles:



0.6 mm particles:



0.7 mm particles:



0.8mm particles:

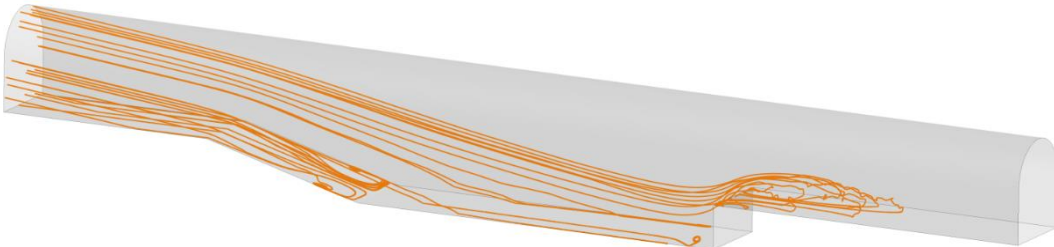


Figure 8.3 Particle trajectories of particle with different diameters in Test Geometry 2.

8.3 Conclusion to the Sediment Transport Study

The results of the analyses performed in this chapter show that Lagrangian Particle Tracking fails to model the bedload transport in a representative way. The particles are not being re-suspended even if they are exposed to flow conditions that would, according to empirical formulas, force the particles up from the bottom. This is an important property of the bedload transport, as the particles in real life roll, jump and slides along the bottom. The suspended particle transport seem to be modelled more correctly, but this is not validated in these analyses.

However, the results of the steady state CFD analyses contain valuable data that can be used to evaluate the particle transport capacity of the tested geometries. The maximum velocity in turbulent eddies and wall shear stress can be applied in empirical formulas and provide critical particle diameter for erosion. These kind of calculations could be performed in the automated CFD application and given as output to the user. In combination with the trajectories of the suspended sediment transport, the user will get valuable information of the transport capabilities of the flow.

9 Pressure Inlet

In most of the analyses in the previous chapters, the inlets are specified as velocity inlets. In some applications, it is beneficial to specify pressure at the inlet and outlet boundaries. This can be challenging with regards to stability in the CFD analyses, and this chapter will contain investigations on how to implement this in the automated solver.

As described in the Theory chapter, the total pressure variable in the ANSYS CFX solver consists of both a static and a dynamic component. Both Total Pressure and Static Pressure can be specified as boundary conditions on the inlet and outlet of the domain. However, in order to get stability, static pressure cannot be used at both inlet and outlet. This is due to the velocity through the domain being undefined. By defining the total pressure on the inlet and static pressure on the outlet, the dynamic component of the total pressure defines the velocity at the inlet. However, this setup can give unwanted start-up effects of the solution, such as backflow was observed at the inlet. These start-up effects may be avoided by adding a large cone shaped inlet, that narrows onto the domain to be analysed.

With the large inlet, the dynamic pressure component is negligible as the velocity on the inlet surface is tending towards zero as the area is increased. With the dynamic pressure almost equal to zero, the total pressure is almost equal to the static pressure. As the flow is contracted into the original domain the flow develops according to the pressure difference between the inlet and outlet. At the outlet of the domain, the total pressure can be measured and subtracted from the inlet pressure to find the total pressure drop over the geometry. By designing the inlet section to be loss free, the pressure loss over the geometry of interest is found. A figurative description of the setup is attached in Appendix D. The next sections will involve the design of such a loss free inlet.

9.1 Geometry, Meshing and Setup

Two different designs of the inlet geometry was analysed. The first geometry involves the creation of a box inlet domain that is suddenly contracted onto the geometry of interest. This type of geometry is easy to implement in the automatic solver. According to theory, a rounded edge at the contraction would lead to the lowest singular losses. Therefore, the contraction edge

was blended to provide a “radius of blended edge/hydraulic diameter”-ratio of 0.25. According to the theory given in Appendix B, this would minimise the head loss. The other suggestion to the inlet geometry was a cone shaped inlet that gradually narrows onto the geometry of interest. According to the list in Appendix B, a cone angle less than 8 degrees will provide a minimal head loss. The inlets was in both cases dimensioned to be 100 times bigger than the cross section area of the geometry of interest. This was assumed to provide a small enough dynamic component of the pressure. Sketches of the geometries are presented in Figure 9.1.

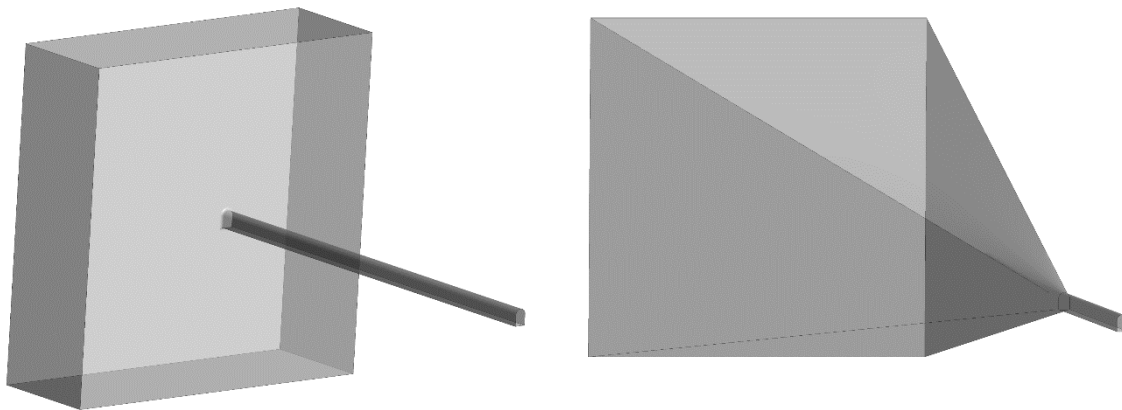


Figure 9.1 Illustration of the geometries used in the total pressure inlet study. The left geometry is a box with a chamfered edge onto the tunnel, which is the geometry of interest. The geometry on the right is the cone inlet that narrows slowly onto the tunnel. The images are not in the same scale and they are just meant to give an overview of the concepts.

Both geometries was built using DesignModeler and meshed in Ansys Meshing with inflation layers and body size to control the total number of elements. A mesh resolution study was performed in order to achieve a mesh independent solution. Total Pressure was applied as inlet boundary condition and a static pressure of zero was applied at the outlet. The walls were modelled as free slip walls in order to avoid friction losses. Using the pressure drop and the related head loss coefficient as parameters of interest a mesh dependency test was performed.

Turbulence decay is likely to occur as the water flows through the inlet domain. At the inlet a turbulence intensity of 5% is specified. This is the default choice in Ansys CFX. In big domains this turbulence intensity is decreased, hence it is feared that the turbulence intensity at the inlet of the geometry of interest will be wrong. Therefore, another simulation was run with 10% turbulence intensity at the inlet boundary, in order to check the significance of turbulence intensity.

9.2 Results and Discussion

The results of the two geometries showed that the cone inlet provided the smallest head loss coefficient at the lowest number of elements in the mesh. See Figure 9.2. The box inlet experienced some backflow out of the inlet in the initial stages of the simulations. However, as the inlet velocity is close to zero this should not have significant impact on the results. Also the cone inlet experienced some backflow, but was stabilised faster and seems more robust than the box inlet. Hence, the cone shaped inlet is considered the best solution for a pressure inlet.

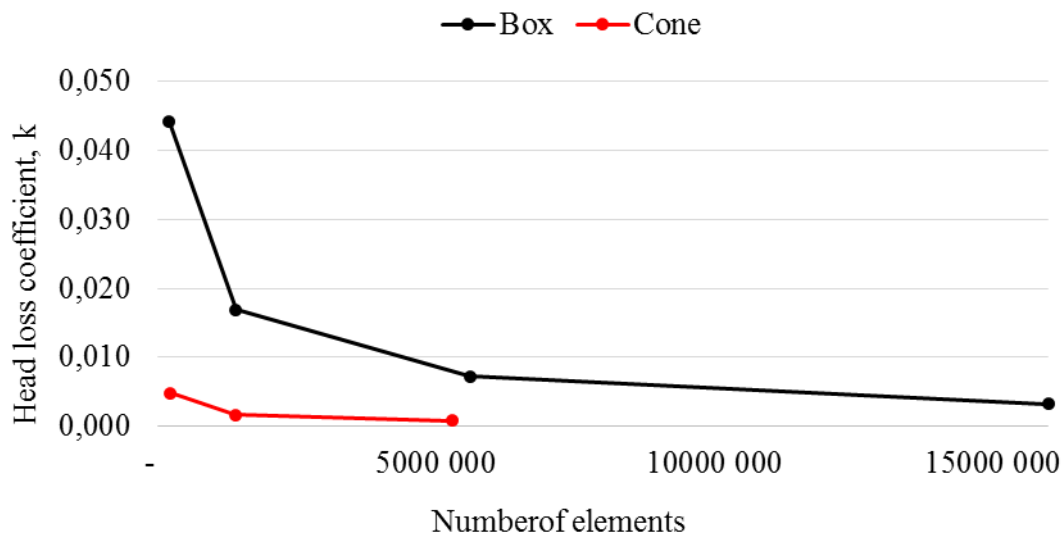


Figure 9.2 Comparison of cone and box inlet.

As expected, the turbulence intensity decay was observed in the inlet geometry. See Figure 9.3 and Figure 9.4. However, when the flow entered the geometry of interest, the turbulence intensity picked up and stabilised at 5% intensity. This also happened when 10% turbulence intensity was specified at the inlet. This implies that it is not necessary to adjust the default settings on turbulence decay, as the turbulence is stabilised in the pipe or tunnel of interest.

The analyses performed in this chapter show that implementation of such a pressure inlet would improve the stability and solution time in the automated solver. However, as it requires input of the total pressure at the inlet and static pressure at the outlet, it might not be applicable in hydropower waterways. In such cases, an estimate for the mass flow rate could be found using total pressure Equation 3.4.

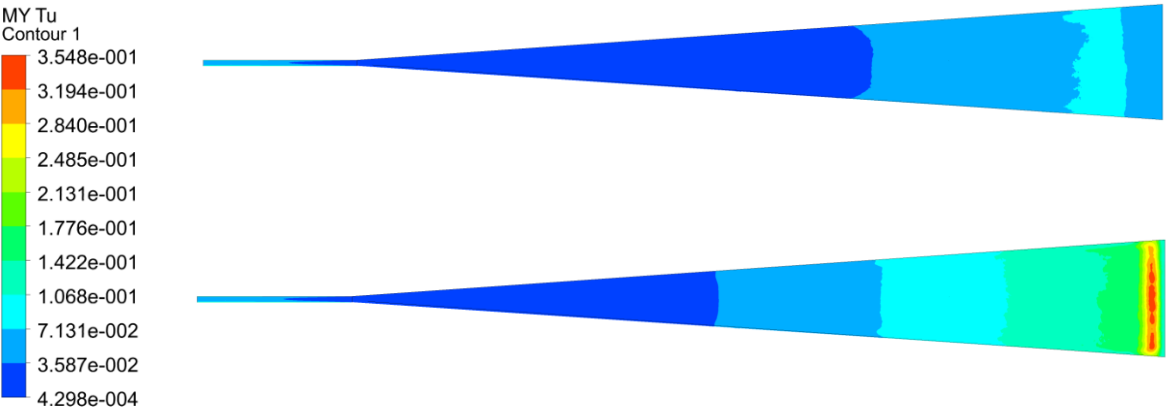


Figure 9.3 Contour plot of turbulence intensity development in the inlet geometry for 5% (upper picture) and 10% (lower picture) turbulence intensity specified on the inlet. Flow direction is from right to left.

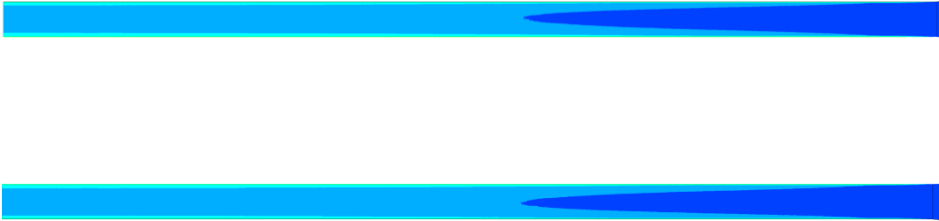


Figure 9.4 Zoomed in on the geometry of interest. Turbulent kinetic energy. 5% (upper picture) and 10% (lower picture) turbulence intensity is specified on the inlet. Flow direction is from right to left.

10 Validation Case

In order to validate the automated solver it was performed an analysis of a sand trap in Tonstad Hydropower station. The Master's thesis of Oddmund Brevik [5] provided geometry drawings and field measurements of the velocity. The field measurements consisted of velocity profiles at three different locations in the sand trap. The velocity profiles were measured with *Acoustic Doppler Current Profilers (ADCP)*. The ADCP measure the velocity of water by transmitting high frequent sound signals into the flow. The sound signals are reflected on particles in the flow, and by utilising the Doppler Effect, the frequency of the returning sound signals can tell the velocity of the particle and its surrounding water [16].

10.1 Geometry, Meshing and Setup

Based on the construction drawings, the geometry was built using the method applied in the automated solver. As the tunnels are blasted out using explosives, the real life tunnel will almost certainly deviate from the construction drawings. Brevik's thesis also provided three scanned cross sections of the tunnel. These was used to adjust the geometry to be as similar to the real case as possible. The geometry can be seen in Figure 10.1. The flow direction is from left to right. The inlet section is extended a little upstream in order to let the flow develop before it enters the sand trap. The cross sectional area of the tunnel expands gradually and the velocity of the water is decreased. On the right hand side of the tunnel looking downstream, there is a transport tunnel used for maintenance reasons. After the sand trap the water passes a trash rack before it is transported into the pressure shafts and down to the turbines. The location of the three ADCP measuring devices is plotted with yellow markers in the figure.

The meshing of the model was performed according to the procedure described in the previous chapters. Inflation layers was applied to get a realistic picture of the flow near walls and a body sizing was applied to control the number of elements. Three meshes (VC-3M, VC-6M and VC-8M) of different level of refinement was created and the details can be seen in Table 10.1. The ratio hydraulic diameter/body size of the mesh elements in the main part of the sand trap, was in the range 37.9-64.0, and hence within the recommended range given in the Mesh Resolution study in Chapter 6.

According to the information from Brevik’s thesis, a uniform flow velocity of 2.65 m/s was specified on the inlet and a static average pressure of zero Pascal on the outlet. The walls were modelled as smooth walls with no slip boundary conditions. The steady state analyses were run utilising SST model for turbulence. The simulations was run until the inlet pressure and the velocity measurements at the three ADCP location had stabilised around an average value.

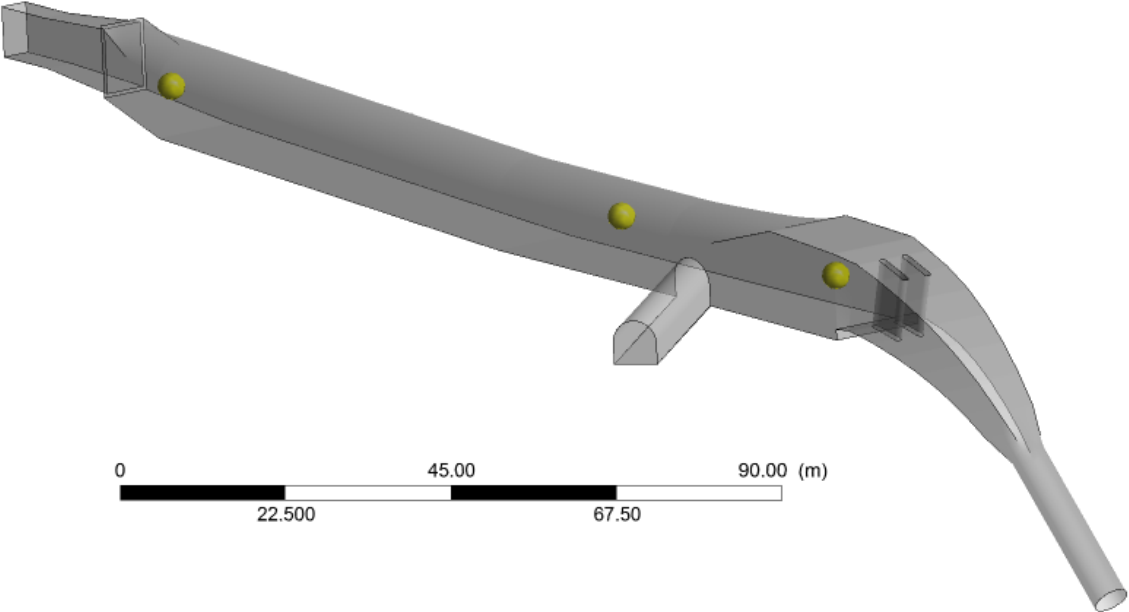


Figure 10.1 Geometry of one of the sand traps at Tonstad hydropower station. The locations of the ADCP monitor points is marked with the yellow balls. ADCP 1 is located at the left, ADCP 2 in the middle and ADCP 3 on the right. The flow direction is from left to right.

Table 10.1 Mesh details of the sand trap analysis of Tonstad Hydropower plant.

Mesh Property	VC-3M	VC-6M	VC-8M
Body Size [m]	0.3	0.23	0.2
First Layer Thickness [m]	4e-3	4e-3	4e-3
Number of nodes	2 834 946	5 554 735	7 974 760
Hydraulic diameter/Body size ratio:			
At ADCP 2	37.9	49.4	56.8
At ADCP 3	42.7	55.7	64.0

10.2 Results and Discussion

The results of the steady state CFD analyses of the sand trap in Tonstad Hydropower station show quite good fit with the velocity field measurements. Comparison of the field measurements and the velocity profiles obtained from the CFD analyses are plotted in Figure 10.2, Figure 10.3 and Figure 10.4 . The magnitude of the maximal velocity appears to be reasonably representative for all of the three measurement points, but the locations of the curves seem to vary among the simulations. An explanation for this can be seen in the monitor plots in Figure 10.5. Especially the velocity at the ADCP 1 location fluctuates quite rapidly. The cross sectional expansion when the flow enters the sand trap creates turbulence that causes these rapid fluctuations of the velocity. Further downstream to ADCP 2 and 3, the flow is stabilised and the velocity is decreased. This can be seen by the smaller amplitude of the velocity fluctuations at ADCP 2 and 3 in Figure 10.5.

The RANS calculated velocity field seem to give the user an indication of the flow pattern. However, turbulent regions, such as the region around ADCP 1, is difficult to model correctly using RANS. With fluctuating velocities, as shown in Figure 10.5, the iteration number at which the analysis is finished is of significance to the solution. The velocity profile seen on ADCP 1 in Figure 10.2 is likely to move between the time steps. Hence, the presented velocity profiles must be interpreted with great caution. In the automated CFD application, the maximum and minimum values should be given as output to the user along with the average results, so that the user could get a stronger foundation to base the conclusions on.

It is important to keep in mind that the results of such an analysis is on a conceptual level. The geometry is built according to construction drawings, but as the blasting of the tunnels can be quite inaccurate, the real life geometry is likely to deviate from the drawings. Certain adjustments can be done, like the pointwise cross sectional adjustment performed in this analysis, but the geometry will never be a perfect replica of the real tunnel. The roughness, which also possibly could make the flow develop differently, is not taken into account. Field measurements of the pressure in the model was not available and hence not validated.

With regards to the mesh quality it can be seen that all of the meshes provided quite good results compared to the field measurements. It is difficult to conclude that the model is mesh independent, because of the velocity fluctuations that is present. However, the guidelines of hydraulic diameter/body size ratio developed in Chapter 6 seem to provide acceptable results.

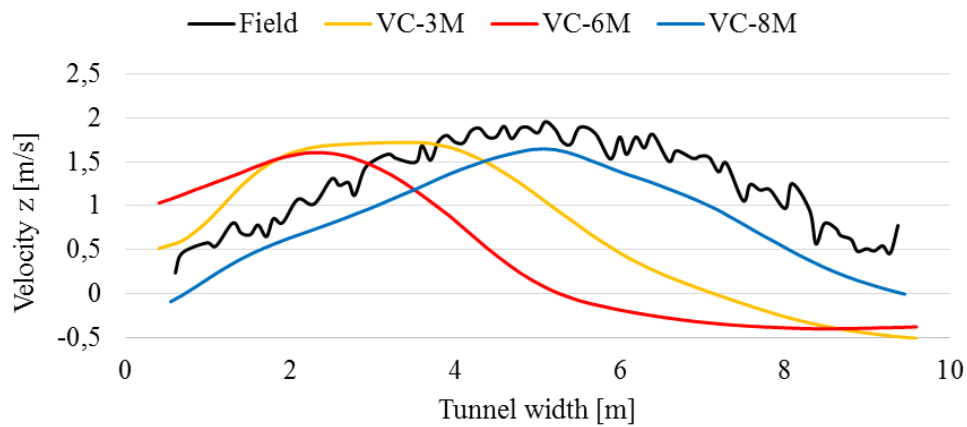


Figure 10.2 Comparison of ADCP 1 velocity measurements and CFD results.

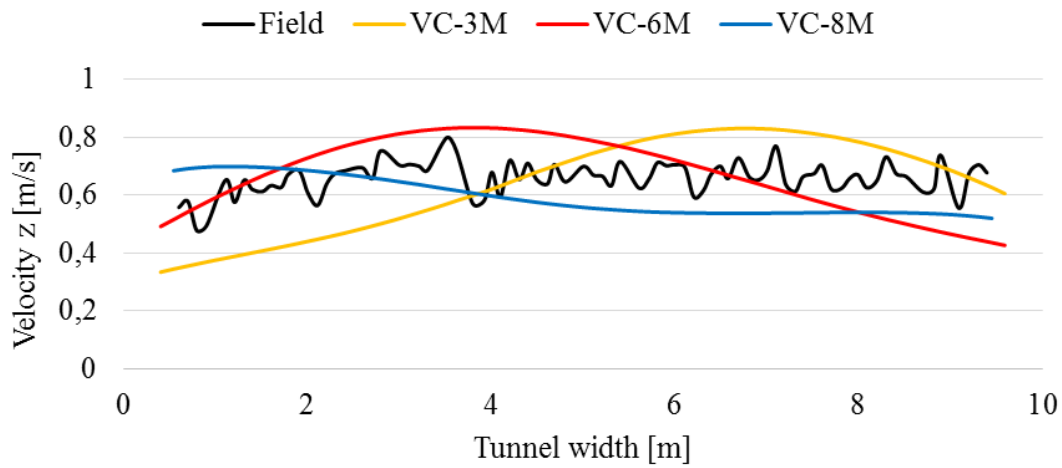


Figure 10.3 Comparison of ADCP 2 velocity measurements and CFD results.

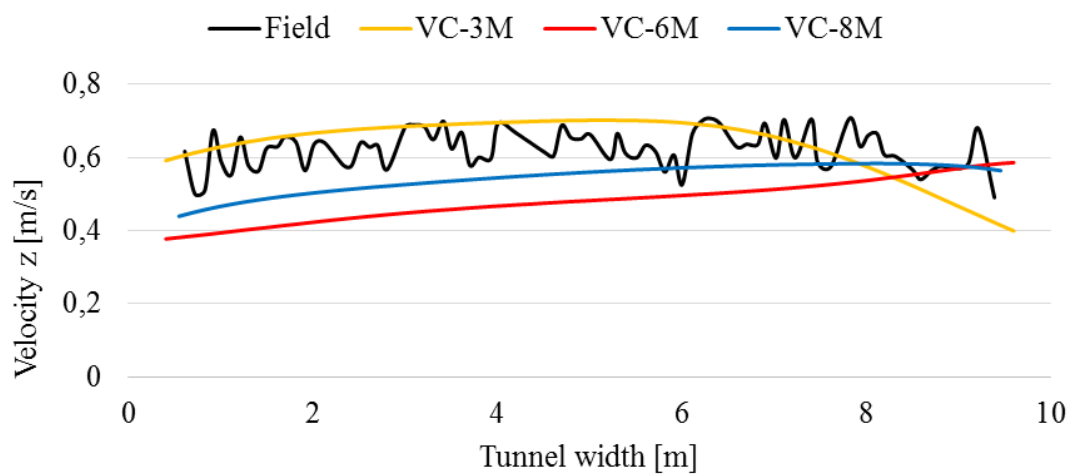


Figure 10.4 Comparison of ADCP 3 velocity measurements and CFD results.

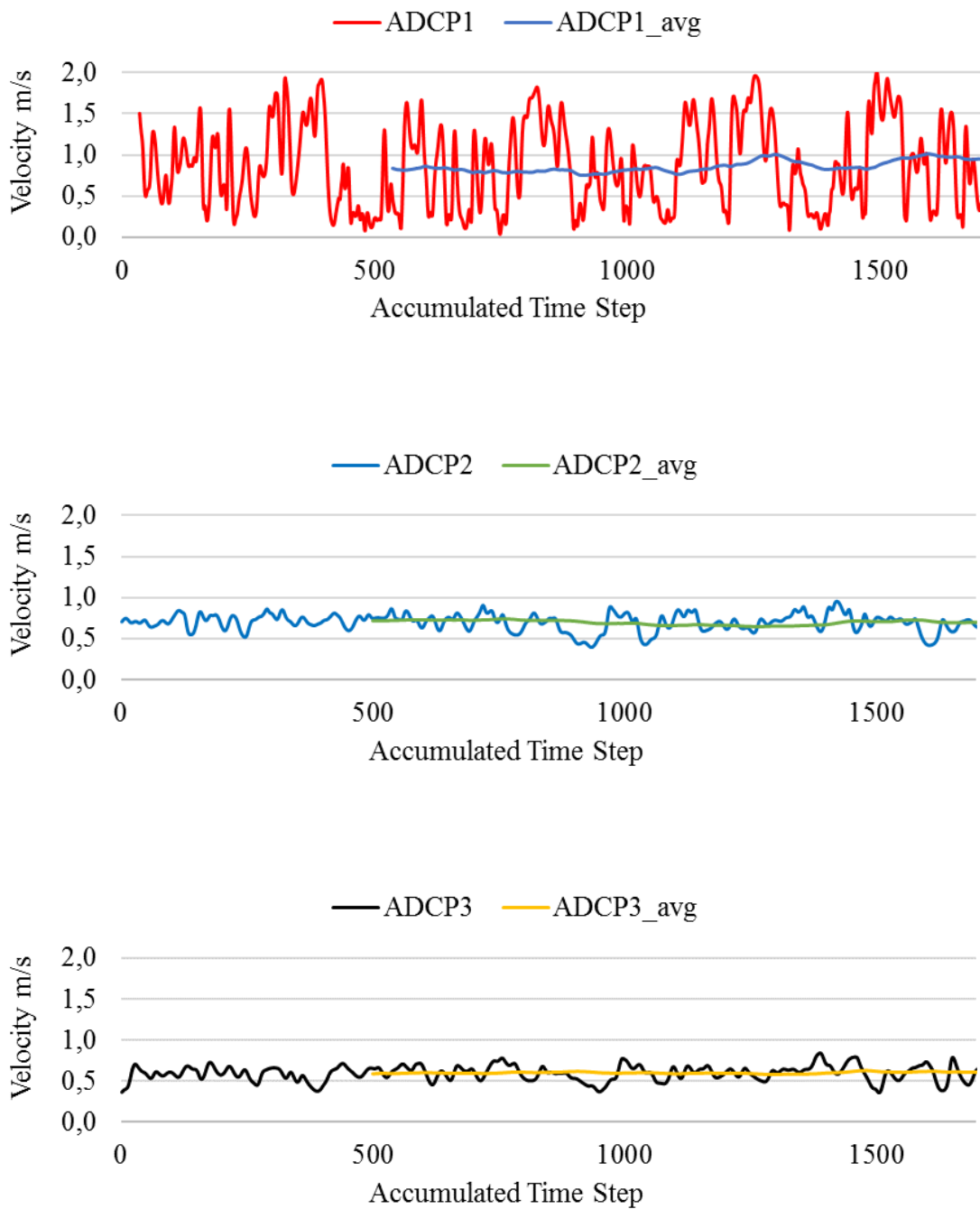


Figure 10.5 Velocity monitor points at the centre of the cross sections at the longitudinal positions of the ADCP measurements. Plotted versus the accumulated time step of the steady state analyses.

11 Conclusion and Further work

The aim of the analyses performed in this master's work was to develop robust methods for an automated CFD application for analyses of the waterways in hydropower systems. The analyses involved a robust mesh generation, the implementation of rough walls and sediment transport analyses, and using pressure as inlet boundary condition. The findings have shown that it should be possible to obtain representative results in order to get a conceptual understanding of the flow in the systems. However, it must be emphasised that the analyses is on a conceptual level and that the results should not be taken as a final answer. The analyses are not meant to replace empirical knowledge and 1D simulations of the waterways, but to be a valuable contribution in the study of local regions of the waterways.

The mesh resolution studies showed that acceptable results can be given with steady state analyses on relatively coarse meshes. A rough estimate of required mesh resolution is given by the “hydraulic radius / cell body size” – ratio. A good starting point of this ratio is found to be in the range between 22 and 64. For most geometries, this would provide an acceptable mesh resolution with regards to both accuracy and computational cost. However, as the geometries analysed may vary largely in complexity, it is recommended to implement a mesh dependence test in the automated CFD application.

In the roughness studies, it was concluded that the CFX built-in rough wall models could not be applied for large scale roughness, such as in blasted hydropower tunnels. The simulation of roughness by resolving the roughness elements with a fine mesh is also not desired in the automatic CFD application, because of the high computational cost. However, the analyses showed that the SST turbulence model is able to provide an acceptable representation of the turbulence in rough surfaced tunnels.

The most promising approach to simulate roughness, is the mesh deformation approach. Analyses showed that the mesh quality was maintained and that the flow field developed as expected near rough walls. However, it was found that the distance between the roughness elements was of significance when it comes to being representative for a certain roughness height. Hence, this would have to be investigated further in order to be applied in the automated CFD application.

The sediment transport study revealed the inability of the Eulerian-Lagrangian approach to model the re-suspension of particles from the bottom of the tunnel. Therefore, the model did not capture the jumping and rolling behaviour of the particle motion along the bottom. This is a critical part to implement in the automated solver, as the bedload transport in hydropower waterways are significant. However, the modelling of suspended sediment transport seemed to be more appropriate. Therefore, in combination with the information about shear stress and velocities near the bed from the CFD analysis, the user will get valuable information about the particle transport capability of the flow.

The pressure inlet study showed that a cone shaped inlet would minimise the head loss related to such an inlet and reduce the start up instabilities. However, the benefit of using such an inlet was questioned, as the required input parameters just as well can be used to estimate a mass flow rate through the domain.

In the validation chapter the methods developed regarding the mesh resolution was applied and the results was compared to field measurements. The results compared well to field measurements. However, the application of steady state analysis with SST model for turbulence does provide some uncertainties regarding the most turbulent regions. Fluctuations in velocity and pressure is significant in the turbulent regions. It is therefore recommended that the user are provided with maximum and minimum values of velocity and pressure together with the average values. That way, the user will have a stronger platform to draw conclusions.

The validation case showed that analyses of waterways could be performed without adding roughness to the walls, and still provide valuable information. Nevertheless, it is important to keep in mind the roughness effects on both velocity and pressure shown in the roughness studies of this thesis.

A natural extension to this project would be to include and develop methods for other geometry details such as trash racks, y-bends and stream intakes. In addition, the implementation of free surface flows would be necessary when studying channels that are only partly filled with water. It is also worth noticing that the principle of the automated CFD application, if it turns out to be successful, would be applicable in several other industries. For instance, the flow in pipelines in the offshore industry or air ducts used for ventilation involves several of the same components as the hydropower waterways.

Bibliography

1. Anna Heiður Eydísardóttir, *Relating measured physical roughness of hydropower waterways to hydraulic roughness*, Master's Thesis, in *Environmental Engineering*. 2013, University of Iceland: Reykjavik.
2. Ansys, *Ansys CFX-Solver Modelling Guide*. ANSYS CFX Release 17.0, 2015.
3. Ansys, *ANSYS CFX-Solver Theory Guide*. ANSYS CFX Release 17.0, 2015.
4. Balakin, B.V., et al., *Eulerian-Eulerian CFD model for the sedimentation of spherical particles in suspension with high particle concentrations*. *Engineering Applications of Computational Fluid Mechanics*, 2010. **4**(1): p. 116-126.
5. Brevik, O., *3D Numerisk modellering av deler av vannvegen til Tonstad kraftverk*, Master's Thesis, in *Bygg- og miljøteknikk*. 2013, NTNU: Trondheim.
6. Bråtveit, K., L. Lia, and N.R.B. Olsen, *An efficient method to describe the geometry and the roughness of an existing unlined hydro power tunnel*. *Energy Procedia*, 2012. **20**: p. 200-206.
7. Cengel, Y.A. and J.M. Cimbala, *Fluid Mechanics: Fundamentals and Applications*. 1st ed. 2006, New York: McGraw-Hill.
8. Chapallaz, J.-M., P. Eichenberger, and G. Fischer, *Manual on pumps used as turbines*. 1992: Vieweg.
9. Cheng, Z. and T.-J. Hsu, *A multi-dimensional two-phase eulerian model for sediment transport—twophaseeulersedfoam (version 1.0)*. 2014, Technical Report No. CACR-14-08, University of Delaware.
10. Det kongelige olje- og energidepartement, *Kraft til endring - Energipolitikken mot 2030*. 2016: Oslo, Norway.
11. Eie, J., *Dammer og kraftverk*. 2 ed. 2000, Bekkestua: NKI forlag.
12. Ferziger, J.H. and M. Peric, *Computational methods for fluid dynamics*. 2012: Springer Science & Business Media.
13. Gimenez, J.M., D. Ramajo, and N.M. Nigro, *Particle Transport in Laminar/Turbulent Flows*. *Meánica Computacional*, 2012. **XXXI**: p. 151-164.
14. Intergovernmental Panel on Climate Change, *Special Report on Renewable Energy Sources and Climate Change Mitigation*. 2012.
15. Launder, B.E. and D. Spalding, *The numerical computation of turbulent flows*. *Computer methods in applied mechanics and engineering*, 1974. **3**(2): p. 269-289.
16. Ocean Instruments. Accessed April 27th 2016;; Available from: <https://www.who.edu/instruments/viewInstrument.do?id=819>.

17. Olsen, N.R. and S. Stokseth, *Three-dimensional numerical modelling of water flow in a river with large bed roughness*. Journal of Hydraulic Research, 1995. **33**(4): p. 571-581.
18. Roalkvam, B.H., *Sandfang i tunneler-Tømming under drift, Master's Thesis*. 2013, NTNU.
19. Rønn, P. and M. Skog. *New method for estimation of head loss in unlined water tunnels. in Hydropower (Conference)*. 1997.
20. Schwimmer, R. Accessed June 1th 2016; Available from: <http://serc.carleton.edu/NAGTWorkshops/sedimentary/activities/14100.html>.
21. Sæterbø, E., L. Syvertsen, and E. Tesaker, *Vassdragshåndboka: håndbok i forbygningsteknikk og vassdragsmiljø*. 1998: Tapir forlag.
22. United Nations, *Paris Agreement, FCCC/CP/2015/L.9/Rev.1*, Framework Convention on Climate Change, Editor. 2015: Paris.
23. Vasquez, J., *Assessing Sediment Movement by CFD Particle Tracking*, in *2nd Joint Federal Interagency Conference*. 2010: Las Vegas.
24. Versteeg, H.K. and W. Malalasekera, *An introduction to computational fluid dynamics: the finite volume method*. 2007: Pearson Education.
25. World Energy Council, *World Energy Resources, 2013 Survey*. 2013, England.

Appendix A MATLAB Roughness Code

```
clear all
clc
hold off

h=6.5; %Height of side walls
r=5.5; %Radius of ceiling arc
z=100; %Length of tunnel section

% Right Wall
[Y,Z,X]=meshgrid(0:0.5:h,0:0.5:z,r);
for i=2:size(X,1)-1
    for j=2:size(X,2)-1
        delta=(-0.5)+1*rand();
        X(i,j)=X(i,j)+delta;
    end
end
surf2stl('rightWall.stl',X,Y,Z)
fig=mesh(X,Y,Z);
hold on
clear X Y Z

%Left Wall
[Y,Z,X]=meshgrid(0:0.5:h,0:0.5:z,-r);
for i=2:size(X,1)-1
    for j=2:size(X,2)-1
        delta=(-0.5)+1*rand();
        X(i,j)=X(i,j)+delta;
    end
end
surf2stl('leftWall.stl',X,Y,Z)
fig=mesh(X,Y,Z);
hold on
clear X Y Z

%Floor
[X,Z,Y]=meshgrid(-r:0.5:r,0:0.5:z,0);
for i=2:size(Y,1)-1
    for j=2:size(Y,2)-1
        delta=(-0.5)+1*rand();
        Y(i,j)=Y(i,j)+delta;
    end
end
surf2stl('floor.stl',X,Y,Z)
fig=mesh(X,Y,Z);
hold on
clear X Y Z

%Ceiling
X=(0:pi/34:pi);
Y=(0:pi/34:pi);
X=r*cos(X);
Y=r*sin(Y);
```

```
Z=zeros(1,35);

for i=1:2*z
    X=[X;X(1,:)];
    Y=[Y;Y(1,:)];
    Z=[Z;Z(1,:)];
    Z(i+1,:)=i/2;
end
Y=Y+h;

for i=2:size(Y,1)-1
    for j=2:size(Y,2)-1

        sinalfa=(Y(i,j)-h)/r;
        cosalfa=X(i,j)/r;
        delta=(-0.5)+1*rand();
        delta_y=sinalfa*delta;
        delta_x=cosalfa*delta;

        Y(i,j)=Y(i,j)+delta_y;
        X(i,j)=X(i,j)+delta_x;
    end
end

surf2stl('ceiling.stl',X,Y,Z);
fig=mesh(X,Y,Z);
hold on
clear X Y Z
```


Appendix B Head Loss Coefficients

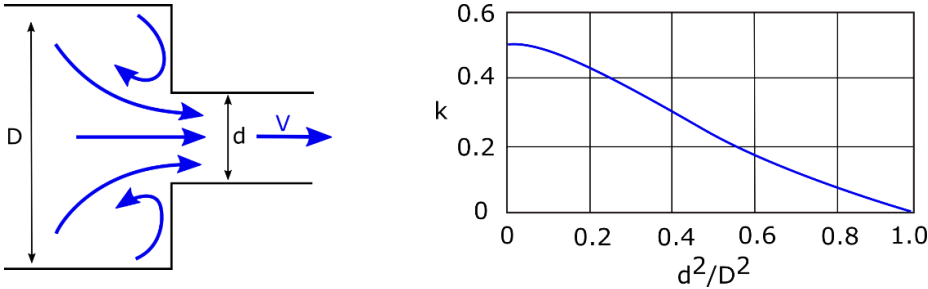


Figure 11.1 Loss coefficient for the sudden contraction of a pipe. Going from a cross sectional diameter, D , to a smaller diameter, d . The head loss coefficient for different ratios of diameters can be seen in the chart on the right [7].

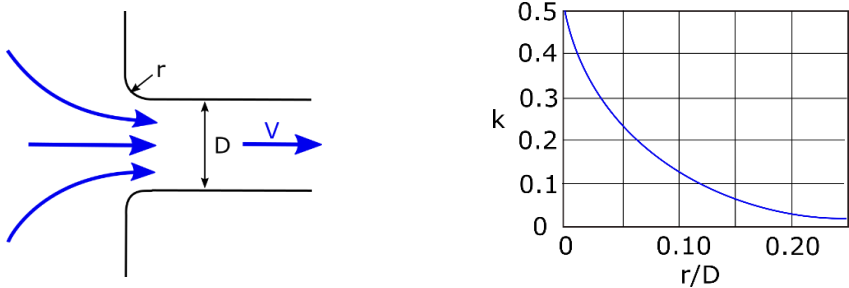


Figure 11.2 Loss coefficients for a rounded inlet. The loss coefficient for various ratios of the rounded radius and diameters is seen in the chart on the right [7].

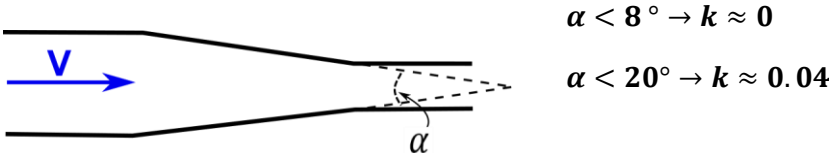


Figure 11.3 Head loss coefficient for a pipe reducer. Loss values for two ranges of reduction angle is listed on the right [8].

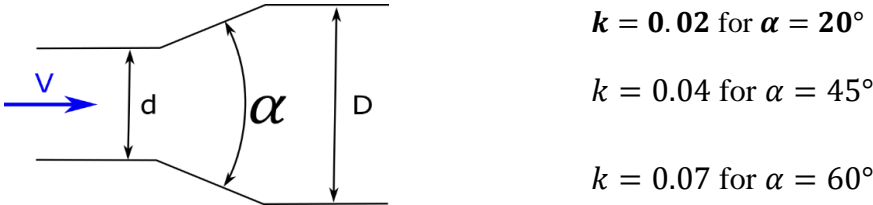
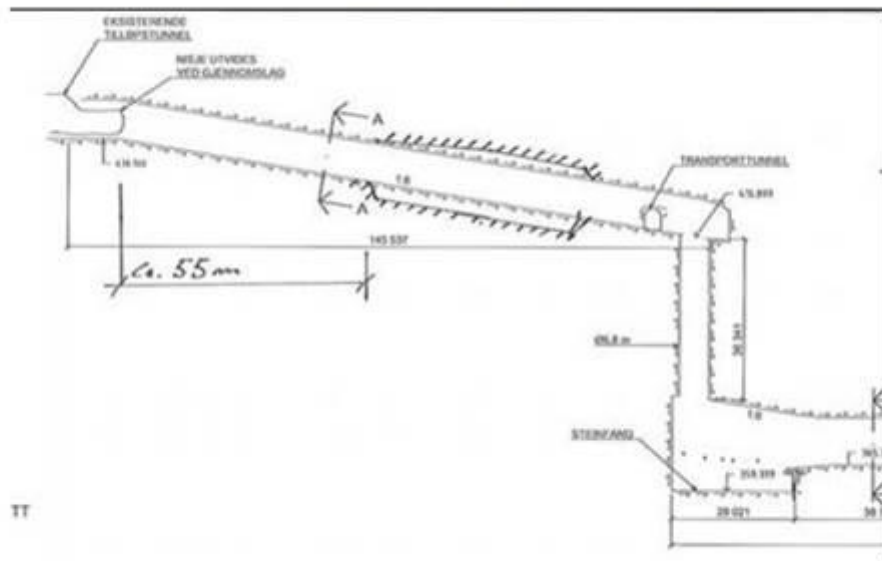


Figure 11.4 Head loss coefficient for a gradual expansion of a pipe. Loss values for a range of expansion angles are given on the right [7].

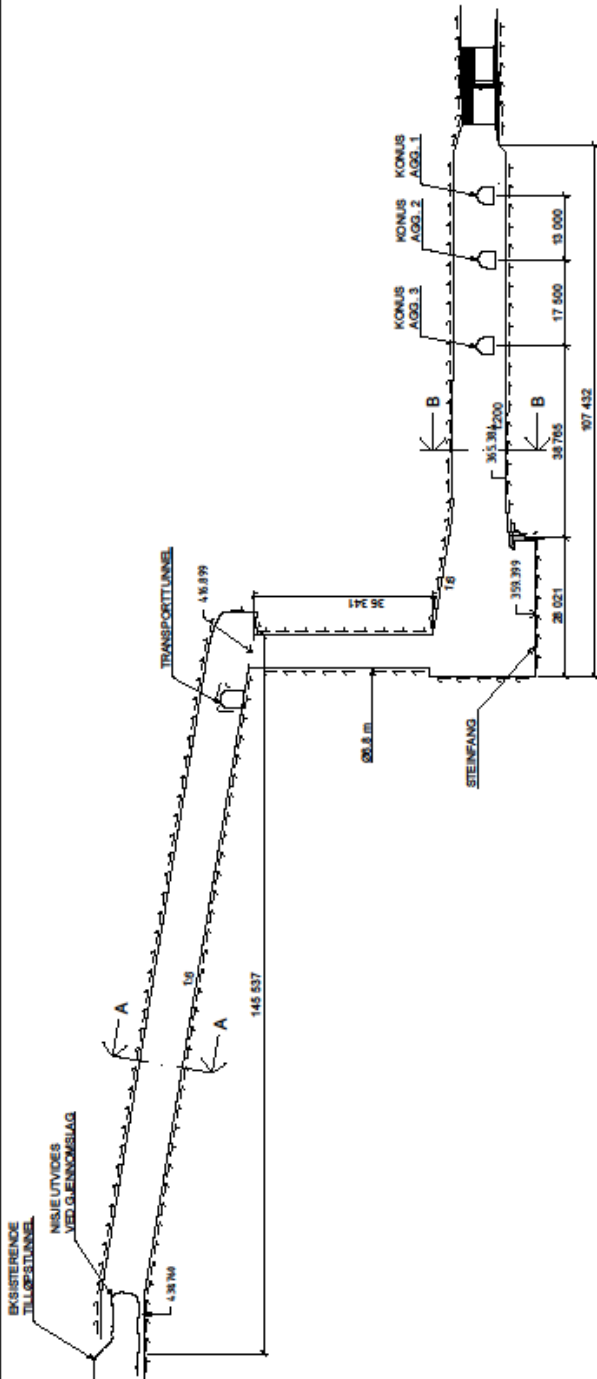
Appendix C Statkraft Drawings

Drawing of the two proposed sand traps at Nore hydropower station. The hand drawn part of the first picture is the Test Geometry 2 and the section at the bottom right is the Test Geometry 3. A more detailed drawing can be inspected on the next page.

Et steinfang med effektivt areal (over avsatt masse) på 90 m^2 vil stoppe partikler større enn ca. 3 mm.



Figur 9 Mulig plassering av steinfang oppstrøms loddsgjaket



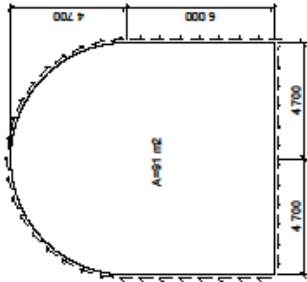
LENDESNIFF
TILØPSTUNNEL
1:500

1973. H.

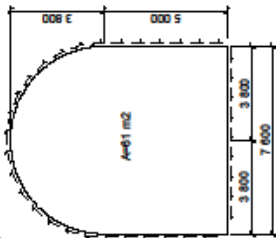
EKISTERENDE TERRENG



LENDESNIFF
UTLØPSTUNNEL
1:1000



SNITT B-B
A=91 m²
1:100



SNITT A-A
TILØP- OG UTLØPSTUNNEL, A=61 m²
1:100



F01 2018-07-31 For anstaltarbeid

ANSK O/E ONE

Som VET

Stordrift

NORE 1 - NYTT KRAFTVERK
TILØP- OG UTLØPSTUNNEL
LENGDE- OG TVERRSNITT
ARRANGEMENT

Nærkontakt 5144614 B010 F01

- HENVISNINGER
1. BOD. TUNNELSYSTEM ØVERSKT
 2. KART GRUNNLAG: ELREFR99 SONE 32
 3. HØYDEGRUNNLAG: NN54

Appendix D Total Pressure Cone Shape

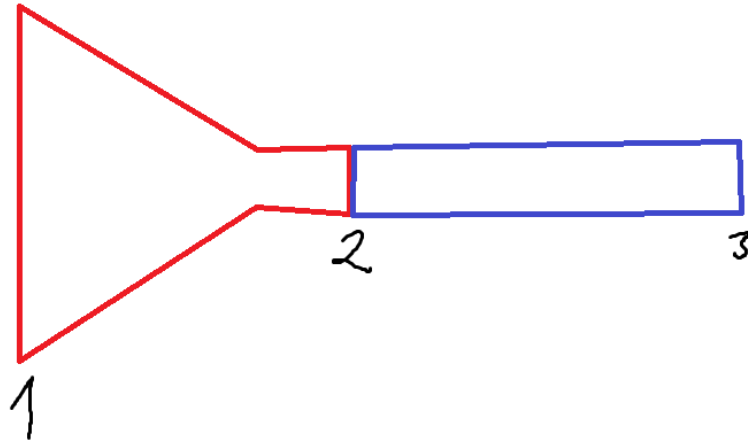


Figure 11.5 Descriptive sketch of total pressure inlet geometry.

The red section constitute the added inlet section. The blue section on the right, between point 2 and 3, is the geometry of interest. The mass flow is unknown, but the total pressure at 2 and static pressure at 3 is known. The inlet 1-2 is designed to have pressure loss close to zero so that the pressure loss, in the geometry of interest can be found in the CFD simulations.

$$\Rightarrow \Delta P_{1-2} = 0$$

$$\Rightarrow \Delta P_{1-3} = \Delta P_{2-3}$$